

# Transparent Graphene-Superconductor Interfaces: Quantum Hall and Zero Field Regimes

Alexey Bondarev,<sup>1</sup> Gu Zhang,<sup>2</sup> and Harold U. Baranger <sup>1, \*</sup>

<sup>1</sup>*Department of Physics, Duke University, P.O. Box 90305, Durham, North Carolina 27708-0305, USA*

<sup>2</sup>*Beijing Academy of Quantum Information Sciences, Beijing 100193, China*

(Dated: 17 February 2025)

We study clean, edge-contacted graphene/superconductor interfaces in both the quantum Hall (QH) and zero field regimes. We find that Andreev reflection is substantially stronger than at an interface with a semiconductor two-dimensional electron gas: the large velocity at graphene’s conical Dirac points makes the requirement of current continuity to a metal much less restrictive. In both our tight-binding and continuum models, we find a wide range of parameters for which Andreev reflection is strong. For a *transparent* interface, we demonstrate the following for graphene in the lowest Landau level QH state: (i) Excellent electron-hole hybridization occurs: the electron and hole components in graphene are simply related by an exchange of sublattice. The spatial profile for the electron component is predominantly gaussian on one sublattice and peaked at the interface, and so very different from the QH edge state of a terminated lattice. (ii) The degree of hybridization is independent of the graphene filling: no fine-tuning is needed. (iii) The spectrum is valley degenerate: the dispersion of each chiral Andreev edge mode (CAEM) self-aligns to be antisymmetric about the center of each valley, independent of filling. Achieving a transparent interface requires the absence of any barrier as well as a superconductor that is suitably matched to graphene; we argue that the latter condition is not very stringent. We further consider the effect of reduced transparency and Zeeman splitting on both the wavefunctions of the CAEM and their dispersion.

## I. INTRODUCTION

### A. Motivation and Context

The interface between graphene and a superconductor has attracted great interest for nearly two decades from several points of view (for reviews see Refs. [1, 2]). First, there has been a long-standing desire for semiconductor-superconductor structures that are gateable and so controllable [3, 4], leading potentially to a variety of interesting quantum devices [5–8]. By encapsulating a graphene sheet between two cladding layers (typically BN), such a high mobility and easily gateable structure can be made from graphene [9–13].

Graphene has a Dirac spectrum at low energy, and so a second motivation has been to investigate how the superconducting proximity effect is manifest in such a material. The Dirac spectrum results from an additional degree of freedom, namely the sublattice A or B in the unit cell of the honeycomb lattice, which can be treated as a Dirac spinor. There are two inequivalent Dirac cones in graphene’s bandstructure, referred to as valleys and labeled  $K$  and  $K'$ . At low energy, this valley degree of freedom can also be treated as a spinor. Thus, the quantum state of graphene may exhibit SU(4) symmetry, which on the other hand may be broken [12]. It has been of interest to study how these degrees of freedom interact with a superconductor in proximity [13–15].

The quantum Hall (QH) effect can be seen in graphene at low magnetic field, of order 1 T. Since the upper crit-

ical field of several thin-film superconductors is of order 10 T, interfaces between graphene in the QH state and several s-wave superconductors have been made [13–19]. This, then, is an interface between very different quantum states: the BCS state of the superconductor with a gap  $\Delta$  and the topological QH state of graphene with a gap of order the inter-Landau-level energy  $E_L$ . Since both systems are gapped, there are no bulk propagating states at the chemical potential. However, there is no obvious gap along the interface, and in fact there are propagating modes confined to the graphene-superconductor interface. We focus on such interface modes, which we call chiral Andreev edge modes (CAEM).

Finally, there has been great interest in interfaces between topological and superconducting states because they can host exotic interface modes [20–22]. For instance, Majorana modes produced in this way [22] could provide a basis for topological quantum computation [23, 24]. The QH/superconductor interface is the simplest interface combining topological and superconducting states, and so provides a first step in this direction.

For all of these reasons there has been substantial work on graphene-superconductor interfaces, starting very soon after the discovery of graphene [1, 2]. A key step was the development of contacts to encapsulated graphene on the edge of the graphene sheet [11]. This allowed for high-quality samples with one-dimensional graphene/superconductor contact [13–19, 25, 26], which is the geometry that we consider here. QH edge and interface modes were observed: a variety of quantum transport properties were studied including the conductance and gating of the CAEM [16–18, 27, 28], interference among them [29, 30], and electrical noise associated with them [31, 32]. In addition the supercurrent in Josephson

---

\* [harold.baranger@duke.edu](mailto:harold.baranger@duke.edu)

junctions in which QH graphene is placed between two superconductors has been studied [15, 19, 33, 34]. Edge-contacted graphene/superconductor has clearly proved to be an excellent, controlled system; its main competitor in QH/superconductor interface physics is the InAs/superconductor system with extended planar contact between the two materials, with which a number of similar quantum transport experiments have been done [35–39].

Theoretical interest in the QH/superconductor system predates the recent experiments [40–49] but has certainly increased because of them. In particular, recent papers [50–63] addressed, for instance, interference among interface modes, effects of sample geometry and disorder, and the roles of dissipation and supercurrent in QH/superconductor hybridization, though not necessarily in the context of graphene.

Our goal in this work is to understand the properties of infinite, uniform graphene/superconductor interfaces in the QH regime, as well as at zero magnetic field. Because the experimental interfaces are thought to be highly transparent [26, 29], we consider interfaces in which the electrons in graphene are coupled strongly to those in the superconductor: there should be no interfacial barrier and the wavefunctions should match well (explained further below). We refer to this situation loosely by saying the interface is “transparent”. For such interfaces, we find that the special properties of graphene lead to new behavior.

## B. Summary of Main Results

We present results for a clean interface between a zigzag edge of graphene in the QH regime and a superconductor, using both continuum and tight-binding models. In both cases we solve the single-particle Bogoliubov-de Gennes equations (BdG) that describe inhomogeneous, mean-field superconductors [1, 64]. In the continuum model, we match wavefunctions between a Dirac spectrum material and one with parabolic dispersion with a large Fermi energy. In the tight-binding approach, we stitch together a honeycomb lattice for the graphene with a square lattice near half filling for the superconductor. The two main assumptions are that (i) there is no disorder in either material or at the interface and (ii) the fields in the BdG equations (the pair potential, one-body potential, and magnetic field) all change abruptly at the graphene-superconductor interface.

Andreev reflection is a convenient way to view the proximity effect in many situations [3, 64–66]. In this approach, one focuses on the excitations on the normal side of the interface. These can be either an electron above the Fermi sea or the absence of an electron below the Fermi sea, namely a hole. Individual excitations cannot propagate into the superconductor; however, two electrons together can connect to the (nearly) zero momentum condensate in the superconductor. In Andreev reflection, an incoming electron with wavevector  $k$  at the

interface pairs with a second electron at  $-k$  and goes into the superconducting condensate. The system therefore has a deficit of  $-k$ , which is described by an outgoing hole with wavevector  $k$ . Thus, the superconductor couples electrons and holes with the same momentum (at the chemical potential). In Andreev reflection in graphene, then, an electron in the  $K$  valley reflects as a hole also in the  $K$  valley. The sublattice structure of this hole is the same as that of the missing  $-k$  electron. Note that this is one of the conventional terminologies [64, 66, 67] but not the only one in general use [1, 59, 65, 68].

The degree of electron-hole hybridization in the mode along the interface is a natural way to characterize the strength of Andreev scattering at high field. Equal weight of electrons and holes in each CAEM means that the proximity effect is maximal (strong Andreev reflection), while weak Andreev reflection leads to modes that are predominately either electron or hole. Quantitatively, we define the “fractional electron content in graphene,”  $f_e$ , by integrating over the electron and hole density in graphene:

$$f_e \equiv \frac{\sum_{\text{sublatt.}} \int_{-\infty}^0 dy |\psi^e(y)|^2}{\sum_{\text{sublatt.}} \int_{-\infty}^0 dy [|\psi^e(y)|^2 + |\psi^h(y)|^2]}, \quad (1)$$

where  $\psi^e$  ( $\psi^h$ ) is the electron (hole) component of the wavefunction. The setup here is that graphene occupies the lower half-plane ( $y < 0$ ) while the superconductor is in the upper. The density on both sublattices (A and B) is included; for lattice models, the integral is replaced by a sum on sites.

Three main conclusions emerge from our study, supported by both continuum and tight-binding results. In this introduction, we use results from the continuum model to briefly illustrate each conclusion in Fig. 1.

First, for a transparent interface, we find strong Andreev reflection—in the quantum Hall regime as well as at zero magnetic field. Current continuity at the interface implies that the ratio of velocities,  $v/v_{FS}$ , is an important parameter (where  $v$  is the velocity at the Dirac point in graphene and  $v_{FS}$  is the Fermi velocity in the superconductor) and that one should have  $v/v_{FS} \sim 1$  for good matching. Since  $v \approx 10^6$  m/sec independent of the graphene chemical potential, achieving this condition is straightforward—unlike for a semiconductor with parabolic dispersion in which the velocity is typically small. We find a wide range of parameters that yield excellent Andreev reflection.

In the QH regime, strong Andreev reflection is illustrated in Fig. 1(a) which shows the transverse wavefunction of the quasi-one-dimensional state at the graphene-superconductor interface in the lowest Landau level (LLL). On the graphene side ( $y < 0$ ), apart from a swap of sublattices, the electron and hole densities are nearly identical, showing that Andreev reflection is strong. Further discussion of the transverse wavefunction appears below in Sec. III B, including for non-ideal cases in V.

Second, we show in Fig. 1(b) that this strong electron-

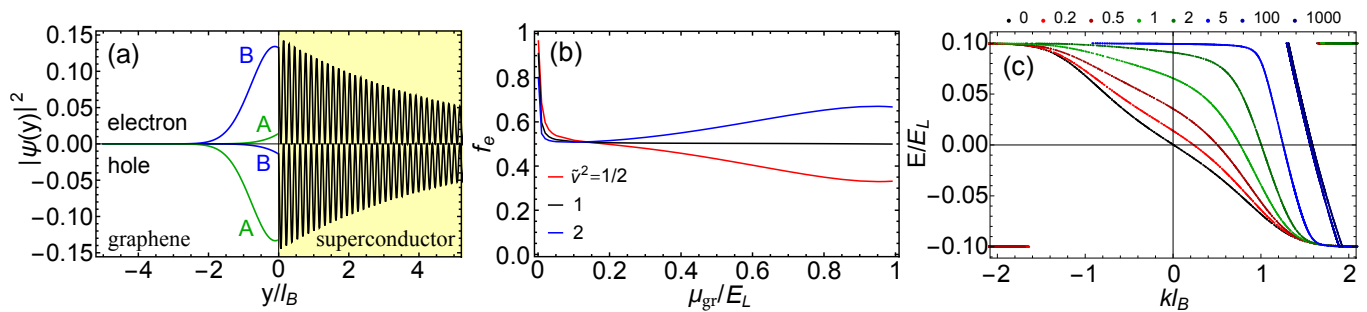


Figure 1. Transparent interface between a superconductor ( $y > 0$ ) and quantum Hall graphene in the LLL ( $y < 0$ ) in the continuum model. **(a) Wavefunction** of the interface mode,  $|\psi(y)|^2$ , in the  $K$  valley: the electron and hole components are plotted as *positive* and *negative* numbers, respectively, and in graphene the sublattice A (B) component is green (blue). In graphene the electron and hole components have the same magnitude, indicating perfect Andreev reflection, but the sublattices are exchanged. **(b) Electron-hole hybridization** expressed as the fractional electron content in graphene [Eq. (1)] as a function of the LLL edge state filling. Shown for three values of the superconductor Fermi energy [cf. Eq. (15) for the definition of  $\tilde{v}^2$ ]. Excellent hybridization is obtained throughout the LLL (except very near the Dirac point). **(c) Dispersion** of the chiral edge mode ( $E < \Delta$ ) for different strengths of the interface barrier (varying  $Z = V_0/\hbar v$  to color-coded values). The spectrum evolves from the terminated-lattice edge mode on the right to the fully-hybridized interface mode centered on the  $K$  point ( $kl_B = 0$ ). (The discontinuities in the spectrum are unrelated to the interface state.) For a transparent interface, then, the spectrum is valley degenerate. (Zigzag edge using standard parameters, see Sec. IID.)

hole hybridization is essentially independent of the chemical potential in graphene. In sharp contrast to the case of a semiconductor with parabolic dispersion [68–71], for a strongly coupled graphene/superconductor interface, strong Andreev reflection is ubiquitous—no fine-tuning is needed. The upper (lower) curve in Fig. 1(b) corresponds to increasing (decreasing) the Fermi energy of the *superconductor* by a factor of two: such a large change in the superconductor causes only a modest change in electron-hole hybridization in graphene. Electron-hole hybridization is discussed further in Secs. IIIB and V.

Third, for a well-matched and transparent interface, the dispersion of the CAEM within the gap of the superconductor is centered on the  $K$  point ( $k=0$ ). The curves in Fig. 1(c) correspond to changing the magnitude of a barrier between the graphene and superconductor: for  $Z = 0$  there is no interfacial barrier, while  $Z \gtrsim 5$  is the tunneling regime. The dispersion evolves from the well-studied QH edge mode for a large barrier (curves on the right) to a mode centered on  $k = 0$  for a completely transparent interface ( $Z = 0$ , black curve) [72]. Indeed, for *all* transparent, well-matched interfaces that we studied (see Sec. IV for further discussion), we find that (i) the dispersion is at the center of the valley at the chemical potential,  $E(k = 0) = 0$ , and (ii) the dispersion is the same in the  $K$  and  $K'$  valleys—it is “valley degenerate”.

The paper is organized as follows. In Sec. II, we introduce the specific continuum and tight-binding models, discuss the approximations, and give our typical values for the model parameters. Sec. III focuses on strong Andreev reflection for transparent interfaces, first at  $B = 0$  and then in the QH regime. In Sec. IV, we discuss the dispersion of the interface modes and the question of valley degeneracy for both perfect and imperfect interfaces. We argue that valley degeneracy, strong Andreev reflection, and strong coupling are naturally connected (Sec. IV D).

The dependence on properties of the superconductor, in particular its chemical potential, are discussed in Sec. V. Though the spin degree of freedom is unimportant in most of our work, in Sec. VI we discuss the Zeeman effect, showing how it breaks perfect hybridization but does not break valley degeneracy. Implications for Majorana modes are discussed. Finally, our conclusions are in Sec. VII, followed by several appendices.

## II. CONTINUUM AND TIGHT-BINDING MODELS OF THE INTERFACE

We approach the graphene-superconductor interface using the standard inhomogeneous mean field theory of superconductivity. The single-particle excitations of the system are conveniently obtained from the Bogoliubov–de Gennes (BdG) equation [1, 64, 66]. One doubles the degrees of freedom in the system by introducing holes and writes a single-particle real-space hamiltonian,  $\mathcal{H}$ , in this doubled (Nambu) space. Concretely, let  $H(\mathbf{r})$  be the normal state hamiltonian with one-body potential  $U(\mathbf{r})$  and magnetic field described by the vector potential  $A(\mathbf{r})$ , and let  $\Delta(\mathbf{r})$  be the superconducting pairing potential (the gap). Then the BdG hamiltonian is

$$\mathcal{H} = \begin{pmatrix} H(\mathbf{r}) & \Delta(\mathbf{r}) \\ \Delta^*(\mathbf{r}) & -H^*(\mathbf{r}) \end{pmatrix}, \quad (2)$$

where energy is measured from the chemical potential. The doubling builds in (artificial) particle-hole symmetry due to redundancy: if the wavefunction  $(\psi^e(\mathbf{r}), \psi^h(\mathbf{r}))$  is a solution with energy  $E$ , then  $(-\psi^{h*}(\mathbf{r}), \psi^{e*}(\mathbf{r}))$  is a solution with energy  $-E$ . In the mean-field BdG equation there are three fields that should be found self-consistently [64]: the superconducting gap  $\Delta(\mathbf{r})$ , the one-body potential  $U(\mathbf{r})$ , and the vector potential  $A(\mathbf{r})$ .

### A. Abrupt Interface: Magnetic, Pairing, and Electrostatic Fields

We make a number of important simplifications with respect to the experimental conditions. First, we take the superconductor to be two dimensional (2D) so that the entire system is 2D. In addition, there is no disorder.

Furthermore, we assume that the self-consistent fields in the BdG approach change abruptly at the graphene-superconductor interface, as commonly done in the literature [42–44, 46, 51–53, 59, 62, 68]. The one-body potential  $U(\mathbf{r})$  certainly changes abruptly when the material changes. We neglect a possible long-range electrostatic contribution to  $U(\mathbf{r})$  caused by charge transfer from the superconductor to graphene. However, the sudden change in the periodic potential is included through a discontinuity in the Fermi energy. Here,  $\mu_{\text{gr}}$  is the chemical potential in graphene measured from the Dirac point, while  $\mu_S$  for the superconductor is measured from the bottom of the band.  $\mu_{\text{gr}}$  and  $\mu_S$  thus denote the Fermi energies as well, and we have  $U(\mathbf{r}) = -\mu_{\text{gr}}$  within graphene and  $= -\mu_S$  within the superconductor [recall that energy is measured from the chemical potential in Eq. (2)].

The pairing interaction vanishes in graphene, implying that  $\Delta(\mathbf{r}) = 0$ . Because the density of states in graphene is much smaller than in the superconductor, the absence of pairing interaction in graphene has little effect on the superconductor. Therefore, in the superconductor we take the magnitude of the gap,  $|\Delta|$ , to be constant. Though  $\Delta(\mathbf{r})$  switches off abruptly at the interface, pairing correlations extend into the graphene, leading to electron-hole hybridization.

The magnetic field,  $B$ , must be large enough to create the quantum Hall state but smaller than the critical field of the superconductor. The superconductor naturally acts to screen the penetration of the magnetic field. With this in mind, we assume that  $B$  drops abruptly from a constant value in graphene to zero in the superconductor, a simplifying approximation that has been used extensively in the literature [42–44, 46, 52, 53, 59, 62]. The abrupt drop of  $B$  implies that the superconductor strongly screens the field, as in bulk type I superconductors. Though the recent experiments involve type II superconductors [29, 31, 38], results from the simple abrupt drop approximation yield general insight into QH-superconductor interfaces. Other work has made a very different simplifying approximation, namely to take  $B$  constant across the interface with no decay [45, 57, 58].

These approximations taken together lead to an enormous simplification of the problem: rather than solving the mean field theory self-consistently, one simply solves the BdG equation once for the fixed, constant values of the potentials:  $\Delta$ ,  $B$ , and the Fermi energies  $\mu_{\text{gr}}$  and  $\mu_S$ . The result is perhaps an overly optimistic picture of the influence of the superconductor on the QH state.

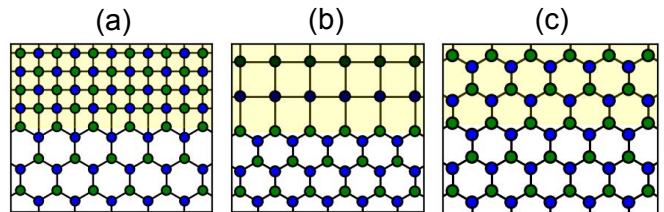


Figure 2. The three graphene-superconductor interfaces studied with the tight-binding model: zigzag edge of graphene stitched to (a) dense, (b) sparse, and (c) honeycomb lattices. The graphene sublattices—green (A) and blue (B)—extend into the superconductor for dense and honeycomb stitching. Atoms on the edge of the graphene sheet are in the A sublattice.

### B. Tight-Binding Model of the Interface

Consider an interface with normal-state hamiltonian

$$H(x, y) = H_S + H_{QH} + H_T, \quad (3)$$

where  $H_S$  represents the superconductor,  $H_{QH}$  the QH graphene, and  $H_T$  the connection between them. The superconductor is described by a tight-binding model on a square lattice in the  $y > 0$  half-plane, and graphene in the QH state is modeled by nearest-neighbor hopping on a honeycomb lattice ( $y \leq 0$ ) with phase factors due to the magnetic field. Details are given in Appendix A.

Since a zigzag edge is thought to be a good model for a generic graphene edge [53, 73, 74], we consider a graphene half-sheet with a zigzag edge (Fig. 2). The graphene half-sheet is translationally invariant in the  $x$  direction with period  $a$ , the lattice constant of graphene (next-nearest-neighbor distance). Our convention is that the sites on the terminal row of the zigzag edge are at  $y = 0$  and belong to the A sublattice. For the magnetic field, we work in the Landau gauge with  $\mathbf{A}(x, y) = By\hat{x}\theta(-y)$  where  $\theta(y)$  is the step function [thus  $\mathbf{B} = -B\hat{z}\theta(-y)$ ]. With these choices,  $\Delta$  is constant and real.

The two materials are joined by matrix elements of magnitude  $t_{NS}$  that connect the graphene and superconductor edge sites. We consider three ways of “stitching” the two lattices together, shown in Fig. 2. First, in the “dense” stitching scenario [Fig. 2(a)], the square lattice of the superconductor has half the period of the graphene lattice and is connected to both graphene sublattices. Second, for “sparse” stitching [Fig. 2(b)], the square lattice has the same period as the zigzag edge and only the terminal A sites are connected to the square lattice [29, 75, 76]. Third, in the “honeycomb” scenario, the graphene lattice is simply continued into the superconductor [Fig. 2(c)], though  $\mu_S$  and  $\mu_{\text{gr}}$  may differ.

The density of states in the superconductor is largest for the dense scenario. Since the period of the square lattice is half that of the zigzag edge, the band structure of the square lattice should be folded back into the smaller graphene (projected) Brillouin zone. Thus the number of bands in the dense case is approximately twice that in the sparse scenario.

### C. Continuum Model of the Interface

In our continuum model, we match a zigzag edge of graphene described by a Dirac hamiltonian to a superconductor with parabolic dispersion. The matching conditions follow from wavefunction and current continuity. The hamiltonian is again given by Eq. (3) where now  $H_T$  denotes a  $\delta$ -function barrier separating the two materials,

$$H_T = V_0 \delta(y). \quad (4)$$

First, for the *superconductor*, we take a 2D free electron model and a constant pairing potential,

$$H_S(x, y > 0) = -\frac{\hbar^2}{2m} \nabla^2 - \mu_S \quad (5)$$

$$\Delta(x, y > 0) = \Delta, \quad (6)$$

where the chemical potential  $\mu_S$  is the Fermi energy and  $\Delta$  is real. For states within the superconducting gap,  $E < \Delta$ , we take plane waves with wavevector  $p$  along the interface and evanescent waves perpendicular to the interface,  $\psi_{S,p}^\beta(y)$  ( $\beta = e$  or  $h$ ), described by a complex wavevector  $q = q' + iq''$ ; see App. A for the exact form. This wavevector is conveniently written in terms of

$$q_y^2 \equiv k_{FS}^2 - p^2 \quad \text{and} \quad q_\Delta^2 \equiv \frac{2m\Delta}{\hbar^2}, \quad (7)$$

where  $k_{FS}$  is the Fermi wavevector of the superconductor. We are particularly interested in the states at the chemical potential,  $E = 0$ , for which we find

$$q^2 = q_y^2 + iq_\Delta^2, \quad (8)$$

$$q = q' + iq'' \approx q_y + i \frac{q_\Delta^2}{2q_y}, \quad (9)$$

where the approximation for the real and imaginary parts of  $q$  in the second line can often be used because  $\Delta$  is usually very small compared to the Fermi energy. The exponential decay length in the superconductor is  $\xi_y \equiv 1/q'' \approx 2q_y/q_\Delta^2 = \hbar v_y/\Delta$ , which we call the coherence length perpendicular to the interface.

Second, for *graphene*, the components of the wavefunction are labeled by sublattice (A or B), valley ( $K$  or  $K'$ ), and electron or hole (denoted  $e$  or  $h$ )— $\psi_{KA}^e(x, y)$ , for example. The hamiltonian in the  $K$  valley is

$$H_{QH}(x, y < 0) = v\boldsymbol{\sigma} \cdot (-i\hbar\nabla + e\mathbf{A}) - \mu_{gr}\sigma_0, \quad (10)$$

where the Pauli matrices  $\sigma_i$  act on the sublattice pseudospin (with  $\sigma_0$  the unit matrix). The corresponding expression for the  $K'$  valley is obtained by the transformation operator  $-i\sigma_y$ . Using the Landau gauge,  $\mathbf{A} = By\hat{x}$ , we look for a plane wave solution proportional to  $e^{ikx}$  where  $k$  is the deviation of the particle's total wavevector from the Dirac point  $K$  or  $K'$ . Solutions perpendicular to the interface, denoted e.g.  $\psi_{KA,k}^e(y)$ , are written in terms of either plane waves ( $B = 0$ ) or parabolic cylinder functions (QH regime [43, 77, 78]), see Appendix A.

The superconducting and quantum Hall forms of the wavefunction must match at the interface. First, because of translational symmetry along  $x$ , the total wavevector must be equal,

$$p = k + K \quad \text{or} \quad p = k + K'. \quad (11)$$

As these two conditions cannot be satisfied simultaneously, the amplitudes for valleys  $K$  and  $K'$  are independent.

Perpendicular to the interface, there are two boundary conditions: both the wavefunction and the current must be continuous for each type of quasiparticle (electron or hole). Since the graphene zigzag edge atoms are on the A sublattice, wavefunction continuity yields

$$\psi_{A,k}^\beta(y = 0^-) = \psi_{S,p}^\beta(y = 0^+), \quad \beta = e \text{ or } h, \quad (12)$$

valid in both the  $K$  and  $K'$  valleys [ $p$  and  $k$  satisfy (11)].

Current continuity constrains the velocity perpendicular to the interface and normally results in continuity of the wavefunction derivative. However, the current operator on the honeycomb lattice [77] relates the amplitudes on the A and B sublattices (nearest neighbors on the honeycomb lattice) and is not a derivative of the A sublattice amplitude. The argument in App. B shows that current continuity yields a boundary condition on the B sublattice:

$$v\psi_{B,k}^\beta(y = 0^-) = \pm \frac{1}{2m} \frac{\hbar}{i} \frac{\partial \psi_{S,p}^\beta}{\partial y} \Big|_{y=0^+}, \quad \beta = e \text{ or } h, \quad (13)$$

where  $+$  is for the  $K$  valley and  $-$  for  $K'$ . When there is a barrier present,  $H_T = V_0\delta(y)$ , it can be incorporated in the boundary conditions by a simple shift in the transverse velocity operator in Eq. (13) [79],

$$\pm \frac{1}{2m} \frac{\hbar}{i} \frac{\partial}{\partial y} \longrightarrow \pm \frac{1}{2m} \frac{\hbar}{i} \frac{\partial}{\partial y} + i \frac{V_0}{\hbar}. \quad (14)$$

Mathematically, the potential barrier increases the imaginary part of the ‘‘momentum’’ along the  $y$  direction, increasing the decay of the wave function across the barrier.

The relative magnitude of graphene's Dirac point velocity to the perpendicular velocity in the superconductor is clearly important for current continuity, Eq. (13). Their ratio is a key parameter below, and so we define

$$\tilde{v}^2 \equiv \left(\frac{v_y}{2v}\right)^2 = \left(\frac{\hbar q_y}{2mv}\right)^2. \quad (15)$$

In terms of the wavevector  $k_0$  of the  $E = 0$  state,

$$\tilde{v}^2 = \frac{1}{4v^2} \frac{\hbar^2 [k_{FS}^2 - (K + k_0)^2]}{m^2} \approx \frac{\hbar^2 (k_{FS}^2 - K^2)}{4v^2 m^2}, \quad (16)$$

where the last approximate expression follows because  $\mu_{gr}$  is not far from the Dirac point and so  $k_0$  is small.

In order to match the wavevector along the interface, Eq. (11),  $\tilde{v}^2 > 0$  is required in order that  $\mu_S > \hbar^2 K^2/2m$ .

Using these boundary conditions in the lowest Landau level spin-degenerate case, we find one solution in each valley,  $E_K(k)$  and  $E_{K'}(k)$  (see App. A for details).

#### D. Regime Studied and Parameter Values

Following the experiments [29–31, 38], we assume a hierarchy of energy scales. Superconductivity is characterized by the smallest scale,  $\Delta$ , and the largest scale is the bandwidth or Fermi energy in the superconductor. The magnetic energy is intermediate: we characterize it by the energy difference between the  $n = 0$  and  $n = 1$  Landau levels, denoted  $E_L \equiv \sqrt{2}\hbar v/l_B$ . In addition, the density of conduction electrons in graphene is much lower than in the superconductor. Thus we consider the regime

$$\Delta \ll E_L, \mu_{\text{gr}} \ll \mu_S. \quad (17)$$

With regard to length scales, the magnetic length ( $l_B^2 = \hbar/eB$ ) should be much larger than the lattice constant in either material. We use a standard set of parameter values for most of the results presented and note any deviations from these standard values.

In the tight-binding model, the hopping matrix element in both the graphene and superconductor is  $t$ . Our standard parameter values are  $t_{NS} = t$ ,  $E_L/t = 0.12$ ,  $\mu_{\text{gr}}/E_L = 1/4$ , and  $\Delta/E_L = 1/10$  [80]. The magnetic length and magnetic field corresponding to this  $E_L$  are  $l_B/a = 10.2$  and  $Ba^2/\Phi_0 = 0.0015$  (or a flux of  $0.0013\Phi_0$  per unit cell, where  $a$  is the lattice constant of graphene). In the superconductor,  $\mu_S$  is typically around half filling, yielding  $\mu_S/t \sim 4$ . (The “optimal values” of  $\mu_S/t$  that we use are 4.5, 5.0, and 0.2 for the dense, sparse, and honeycomb lattices, respectively.) Thus the Fermi energy in graphene is much smaller than that in the superconductor:  $\mu_{\text{gr}}/\mu_S \sim 0.01$ .

In the continuum model, the most important parameter is the velocity ratio (15) entering the current continuity boundary condition: our standard value is  $\tilde{v}^2 = 1$ , which corresponds to perfect matching. The strength of the superconductivity is set by  $\Delta = 0.01(2mv^2)$ , ensuring slow evanescent decay in the superconductor,  $\xi_y q_y = 200$  in the approximation of Eq. (9). The magnetic field is fixed by either  $\xi_y/l_B = 10$  or  $\Delta/E_L = 0.1$ , which differ by only a factor of  $\sqrt{2}$ . We use quarter filling of the LLL edge state as our standard doping,  $\mu_{\text{gr}}/E_L = 1/4$ , and no graphene-superconductor barrier,  $V_0 = 0$ .

In the absence of spin-orbit coupling and the Zeeman effect, the problem decouples into two independent, identical problems, leading to doubly degenerate states. We therefore neglect spin until Zeeman effects are discussed in Sec. VI.

### III. STRONG ANDREEV REFLECTION

We start by demonstrating that it is possible to get strong Andreev reflection at a graphene-superconductor interface, both at  $B = 0$  and in the quantum Hall regime, despite the abrupt change in material and the very large mismatch in the density of states. This stands in sharp contrast to the well-established result for semiconductor-superconductor interfaces (for parabolic dispersion in both) in which the probability of Andreev reflection is small (except for special fine-tuned cases) [42, 45, 68–71, 81]. For clarity, we focus on only a few values of parameters in this section and postpone (Secs. IV and V) a discussion of the sensitivity to model parameters.

#### A. $B = 0$ : Robust Andreev Reflection and the Dirac Point Velocity

Before turning to the QH regime, it is instructive to consider the  $B = 0$  case. An electron incident on the interface will be reflected as either an electron or hole. The probability of Andreev reflection follows from wavefunction matching. This was done for an interface between free-electron materials (parabolic dispersion) in the classic work by Blonder, Tinkham, and Klapwijk (BTK) [68, 69]. Here we perform a similar analysis for an interface between graphene described by the continuum Dirac equation, Eq. (10) with  $\mathbf{A} = 0$ , and a superconductor with parabolic dispersion, Eq. (5).

The form of the wavefunction in the superconductor does not depend on  $B$  and so is the same as in the previous section. On the graphene side, we continue to look for a solution proportional to  $e^{ikx}$  but now the solution should be plane wave perpendicular to the interface as well, with an ingoing electron state and outgoing electron and hole states. The calculation is presented in App. C, together with additional results.

The main feature is already evident in the simple case of normal incidence in the limit  $q_\Delta \ll q_y$ . In this limit, Eq. (9) implies that the imaginary part of  $q$  can be neglected in the boundary conditions. We find in this case that the probability of Andreev reflection is

$$P_A = \frac{4\tilde{v}^2}{(1 + \tilde{v}^2)^2}, \quad (18)$$

where  $\tilde{v}$  is the ratio of velocities defined in Eqs. (15)–(16). The functional dependence here is striking: there is a broad maximum of perfect Andreev reflection at  $\tilde{v}^2 = 1$ , while  $P_A \rightarrow 0$  in the two limits  $\tilde{v}^2 \rightarrow 0$  and  $\tilde{v}^2 \rightarrow \infty$ . The characteristics of the superconductor enter through a somewhat weak dependence on the transverse velocity  $v_y$ —note that  $k_{FS}$  and  $K$  do not enter independently. The key point, however, is that the dependence on  $k_0$ , and thus on  $\mu_{\text{gr}}$ , in (16) is very weak. The wavelength of the particles in graphene plays almost no role. *Andreev reflection in clean graphene is determined by the properties of the superconductor and the conical valley structure*

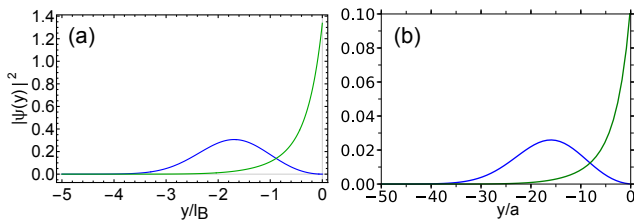


Figure 3. QH edge states of a terminated graphene lattice (zigzag edge) in the (a) continuum and (b) tight-binding models. The wavefunction of the  $K$ -valley mode,  $|\psi_K(y)|^2$ , on the A (green) and B (blue) sublattices is shown. (Standard parameters, Sec. IID.)

of graphene—the value of  $K$  and, most importantly, the velocity at the Dirac point.

Quantitatively, the velocity at the Dirac point in graphene is of the same order as the Fermi velocity in metals, so from (18) we can expect situations in which there is very good Andreev reflection,

$$\tilde{v} \sim 1 \quad \text{and} \quad P_A \lesssim 1, \quad (19)$$

even for a large mismatch between the graphene and the superconductor,  $\mu_{\text{gr}} \ll \mu_{\text{FS}}$ . While these results are for the simplest case of normal incidence neglecting the effect of  $q_\Delta$ , results in App. C go beyond those assumptions and show that the conclusion is general.

This is very different from Andreev reflection in a semiconductor with parabolic dispersion. In that case, the big mismatch between the velocities in the semiconductor and the superconductor suppresses Andreev reflection strongly. Indeed, with the same simplifications as for graphene above, the result for a clean semiconductor-superconductor interface is

$$P_A \approx \frac{4}{\tilde{v}^2} = 4 \frac{m_S \mu_{\text{FN}}}{m_N \mu_{\text{FS}}} \ll 1, \quad (20)$$

where  $N$  denotes the semiconductor [68–71]. Thus, the conical valleys in graphene allow much better connection to superconductors than for semiconductors with comparable density; indeed, in graphene there is the possibility of near perfect Andreev reflection.

## B. Quantum Hall Regime: Good Electron-Hole Hybridization

In this subsection, we show that good electron-hole hybridization in the QH regime is possible. By “good hybridization” we mean that the weight of electrons and holes in each CAEM wavefunction are nearly equal [ $f_e \approx 0.5$ , see Eq. (1)].

### 1. QH Edge States on a Terminated Lattice

We start with the QH states on the graphene edge in the absence of a superconductor—that is, when the

lattice is abruptly terminated. The electron states in this case are well-known for both the tight-binding and continuum models [77, 78, 82–85].

In the bulk, the LLL states have energy zero (with respect to the Dirac point). In the Landau gauge used here, the wavefunctions are plane waves in  $x$  and a simple Gaussian in  $y$  around a guiding center  $\bar{y}(k)$ . For each guiding center position, there are two solutions corresponding to measuring  $k$  from either  $K$  or  $K'$ . Importantly, there is “sublattice-valley locking”: solutions associated with valley  $K$  are on the B sublattice exclusively and those associated with  $K'$  are on the A sublattice.

When  $\bar{y}$  approaches the edge, boundary conditions come into play. In our geometry the boundary condition is that  $\psi$  on the B sublattice must be zero (i.e. the absent next row in the lattice). Since the  $K'$  valley states are non-zero only on A sites, they are not modified: their energy remains strictly zero.

In contrast, the  $K$  valley wavefunctions reside on the B sites and must go to zero faster at the edge than in the bulk, changing their energy. Thus, the LLL edge mode at the chemical potential corresponds to an electron in the  $K$  valley. With the change in  $\psi$  on B sites, there must be amplitude on A sites in order to satisfy the coupled equations. The wavefunction is shown for both the continuum and tight-binding models in Fig. 3; results of the two approaches are in very good agreement.

### 2. Interface wave function: Continuum model

For the continuum model at  $B = 0$ , we found perfect Andreev reflection if the superconductor and graphene are well matched,  $\tilde{v}^2 \approx 1$ . The corresponding wavefunction in the QH regime is shown in Figs. 1(a) and 4 for  $\tilde{v}^2 = 1$ . Strikingly, the magnitude and spatial dependence of the electron component in graphene ( $y < 0$ ) are the same as those of the holes, except that the sublattice components are interchanged. Evidently in this case, Andreev reflection in the QH regime is also perfect.

The wavefunction in graphene is clearly very different from that for a terminated lattice (Fig. 3). Here, the

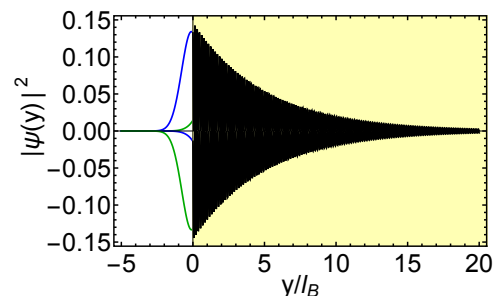


Figure 4. Wavefunction of the interface mode,  $|\psi(y)|^2$ , in the continuum model for ideal graphene-superconductor matching: for  $E = 0$  in the  $K$  valley as in Fig. 1(a), but on an expanded scale to show the evanescent decay into the superconductor (Standard parameters, Sec. IID.)

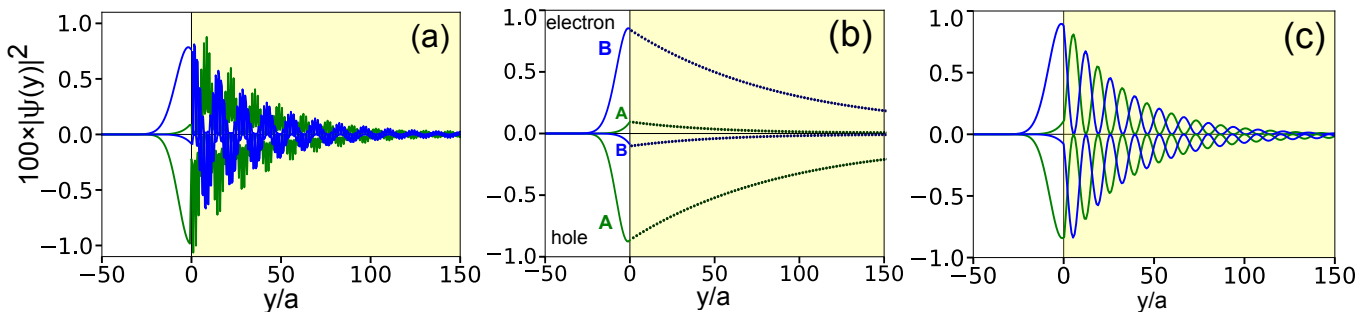


Figure 5. Mode wavefunctions,  $|\psi(y)|^2$ , at the chemical potential ( $E = 0$ ) in the  $K$ -valley for three well-matched tight-binding interfaces: (a) dense, (b) sparse, and (c) honeycomb superconductor (shown in Fig. 2). The electron and hole components are plotted as positive and negative numbers, respectively, and green (blue) refers to the A (B) sublattice. All three interfaces are highly transparent, achieved using  $t_{NS}/t = 1$  and  $\mu_S/t =$  (a) 3.8, (b) 5, and (c) 0.2. In panel (b) for  $y > 0$ , dark green and blue denote the even and odd rows of the square lattice counting from the interface. The degree of  $e$ - $h$  hybridization is given in Table I. (Standard parameters, Sec. IID.)

electron resides mostly on one sublattice (B, blue)—that of the bulk,  $K$ -valley LLL wavefunction—and is Gaussian shaped, centered slightly left of the interface, and cut at  $y = 0$ . The deviation from gaussianity produces the small amplitude exponential decay on sublattice A.

In the hole component, the roles of sublattices A and B are reversed. Because the sublattice structure is different, the hole component here *cannot* represent the absence of the same type of electron as in the electron component, namely a  $K$ -valley electron. Rather, the hole component is similar to the bulk LLL wavefunction for the  $K'$  valley which is on the A sublattice (sublattice-valley locking). Thus, a  $K$ -valley electron has been paired with a  $K'$  valley electron, as expected for a Cooper pair.

Three length scales are visible in the wavefunction. (i) The magnetic length,  $l_B$ , sets the scale of variation in the quantum Hall state. (ii) The Fermi wavelength in the superconductor sets the scale for the rapid oscillations at  $y > 0$ . (iii) The scale of the slowly decaying envelope in the superconductor is given by the coherence length  $\propto 1/\Delta$  [86].

The filling of the edge state,  $\mu_{gr}/E_L$ , plays little role in the matching. Indeed, for a suitable superconductor for which  $\tilde{v}^2 \approx 1$ , the degree of electron-hole hybridization is essentially independent of  $\mu_{gr}$ . The fractional electron content in graphene,  $f_e$  in Eq. (1), is one way to quantify the  $e$ - $h$  hybridization. Fig. 1(b) shows  $f_e$  in the LLL as  $\mu_{gr}$  varies from the Dirac point to the threshold for the first Landau level,  $E_L$ . For  $\tilde{v}^2 = 1$ , hybridization is perfect,  $f_e = 1/2$ , throughout the LLL.

### 3. Interface wave function: Tight-binding model

Our tight-binding results corroborate the features found in the continuum limit. The wavefunctions for the three superconductor models are shown in Fig. 5. In each case we have chosen the Fermi energy in the superconductor to achieve very good matching to the graphene, and the transparency of the interface is about 85%. (By “transparency” here we mean specifically the transmis-

Fig. (panel)	Fractional electron content, $f_e$	Deviation from valley center, $\delta k_0 l_B$
3(c)	1.0	1.49
5(a)	0.50	0.10
5(b)	0.49	0.02
5(c)	0.54	0.05
12(a)	0.82	0.40
12(b)	0.78	0.37

Table I. For the tight-binding wave functions shown in Figs. 3, 5, and 12, we give the fractional electron content in graphene [ $e$ - $h$  hybridization, Eq. (1)] and the deviation of the wavevector  $k_0$  for the  $E = 0$  mode from the center of the  $K$  valley:  $\delta k_0 l_B \equiv (k_0 - K)l_B$ .

sion probability at  $B=0$  in the normal state [87].) Note that there is nearly equal weight of electrons and holes in graphene. Indeed, on both sides of the interface and in all three cases, the hole component is directly related to the electron component by simply interchanging the A and B sublattices.

It is clear from the plots that there is excellent global electron-hole hybridization. Quantitatively, the value of  $f_e$  is found from the wavefunction [see Eqs. (1) and (A6)] and reported in Table I. They are  $\approx 0.5$  and so nearly ideal. However, we wish to emphasize a more striking feature: if we consider the sum of the A and B site weights, the spatial profile of the electron and hole components is nearly the same. Thus, there is excellent electron-hole hybridization in every graphene unit cell.

On the graphene QH side ( $y < 0$ ), the wavefunction for each stitching has all the characteristics of the continuum. The B sublattice predominates in the electron component, corresponding to the bulk LLL state in the  $K$  valley, and the shape of the B-sublattice component is close to that of a bulk wavefunction. To be consistent,  $\psi(y)$  on the A sublattice is small, in contrast to the QH edge state [Fig. 3(b)]. In the hole component, the two sublattices are interchanged. The shapes of the electron and hole components are very similar but not identical—

the fact that the QH side terminates in A sites breaks the symmetry.

On the superconductor side ( $y > 0$ ), the three cases are similar despite the different underlying lattices. First, the exponential decay of the envelope of oscillations is controlled by the magnitude of the superconducting gap,  $\xi_y \approx \hbar v_y / \Delta$ , as in the continuum model. In the honeycomb-lattice superconductor, panel (c), the sublattice structure extends into the superconductor, and oscillations corresponding to the transverse wavevector occur with a period shorter than  $l_B$  because  $\mu_S > \mu_{gr}$ . The fact that the oscillations on the A and B sublattice are out of phase is connected to the big difference in weight of the two sublattices on the QH side.

The square lattice is bipartite, of course, and for dense-stitching, the bipartite nature on the two sides of the interface match [see Fig. 2(a)]. Thus, panel (a) shows oscillating sublattice weights in the superconductor, much as in (c). The very fast oscillation is the wavelength in the superconductor: since  $\mu_S$  is near half filling,  $\lambda_{FS}$  is on the lattice scale.

With sparse stitching, there is only one square lattice site per graphene unit cell and so once stitched together the lattice is not bipartite. Focusing on a unit cell of the interface, however, we see that the square lattice consists of a single chain of sites, and so the bipartite structure is reduced to even-odd alternation. Indeed, in panel (b), the wavefunction oscillates rapidly between even and odd rows in the superconductor ( $\mu_S$  is near half filling) [88]. It is particularly striking that the electron and hole weights for  $y > 0$  are exactly out of phase.

#### IV. DISPERSION OF CHIRAL ANDREEV EDGE MODES: VALLEY DEGENERACY?

Having established the possibility of strong hybridization in the CAEM, we now further investigate their properties through the spectrum of states.

##### A. QH Terminated-Lattice Spectrum

Before discussing the spectrum of the interface itself, we present the BdG spectrum for an abruptly terminated honeycomb lattice in the QH regime. The spectrum of the electron solutions is well-known [77, 78, 82–85]. To obtain the hole spectrum from the electrons, the particle-hole symmetry of the BdG equation implies that one inverts both the crystal momentum and the energy [67],

$$K + k \rightarrow K' - k \quad \text{and} \quad E \rightarrow -E. \quad (21)$$

The spectrum with both electrons and holes is shown in Fig. 6 [89]. In the continuum solution, panels (a)-(b), both the electron mode at the chemical potential in the  $K$  valley and the corresponding hole mode in  $K'$  are clearly seen. Since the LLL  $K'$  valley states are not modified by the termination of the lattice (they are non-zero only

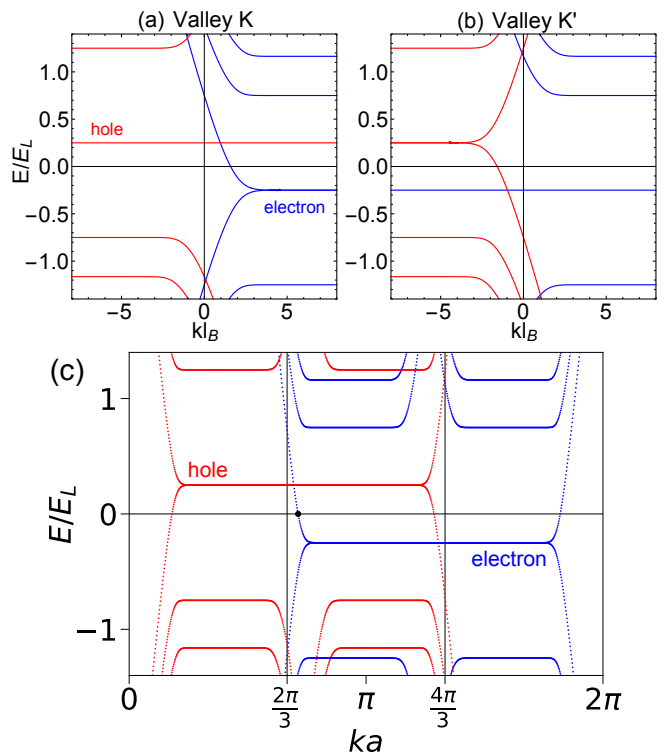


Figure 6. Spectrum of electron (blue) and hole (red) states for a zigzag nanoribbon in the QH regime. (a)-(b) Continuum model for the  $K$  and  $K'$  valley, respectively. (c) Tight-binding results: the Brillouin zone is shifted to  $[0, 2\pi/a]$ , and the hole spectrum is translated by a reciprocal lattice vector into this interval. The point marks the electron edge state,  $E(k_0) = 0$ . The value of  $k_0$  given in Table I shows that this state is located  $\sim l_B$  inside the graphene [wavefunction shown in Fig. 3(b)]. (Standard parameters, Sec. III D.)

on A sites), their energy remains zero: they appear as horizontal blue lines in panel (b). Due to this flat band, while there is no hole state in the  $K$  valley at the chemical potential (no red line crosses  $E = 0$ ), the electron and hole solutions do intersect at  $E = \mu_{gr}$ .

For the tight-binding results, panel (c), periodicity in the  $x$  direction leads to a Brillouin zone of size  $2\pi/a$ . We show the interval  $k \in [0, 2\pi/a]$  in which the Dirac points are  $Ka = 2\pi/3$  and  $K'a = 4\pi/3$ . To focus on the  $y = 0$  edge of the nanoribbon, the width of the nanoribbon,  $W$ , is chosen so that the spectrum of the states on the other edge is clearly separated:  $W \lesssim l_B^2 (4\pi/3a)$  [90].

At the chemical potential, there is an electron state in the  $K$  valley and a hole in  $K'$ . Note that the spectrum near the Dirac points is very similar to that of the continuum model (see also the zoom near the  $K$  point in Sec. D 1). The tight-binding solution shows how the two valleys are connected through the  $M$  point,  $ka = \pi$ .

##### B. Implications for Andreev Reflection

From these results on a terminated lattice, *what can we anticipate for the interface with a superconductor?*

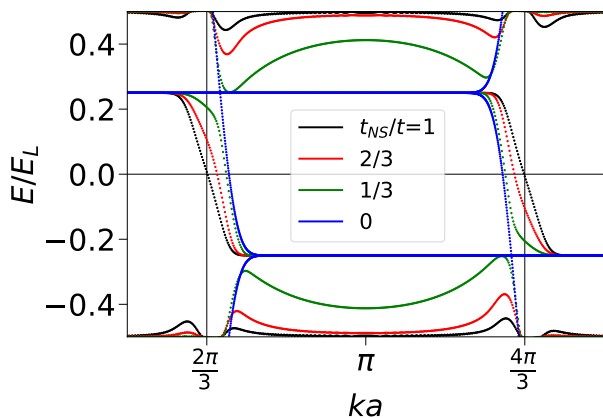


Figure 7. Edge mode dispersion for different strengths of coupling to the superconductor: tight-binding results for sparse stitching and large pairing gap  $\Delta/E_L = 0.5$  ( $\Delta > \mu_{\text{gr}}$ ). The values  $t_{NS}/t \in \{0, 1/3, 2/3, 1\}$  correspond to interface transparency  $\{0, 0.25, 0.7, 0.85\}$ , respectively [87]. The spectrum evolves from the terminated-lattice edge mode to the fully-hybridized interface mode centered on the  $K$  point. (Otherwise standard parameters, Sec. II D.)

At first sight, the case for a strong proximity effect appears hopeless: we should look for electron and hole states that (i) have the same crystal momentum (translational invariance), (ii) overlap spatially in the transverse direction (local interaction), and (iii) differ in energy by  $\lesssim \Delta$  (matrix element of superconductivity that mixes electrons and holes). These criteria are *never* satisfied in Fig. 6: there is no crossing of the electron and hole modes at the chemical potential. Such a crossing is achieved only through fine tuning to  $\mu_{\text{gr}}/E_L = 1$ .

One clear scenario that avoids this dead end is to abandon the assumption of a clean system [53, 57]. Disorder breaks translational invariance, thus removing criterion (i) above, allowing the  $E = 0$   $K$ -valley electron and  $K'$ -valley hole in Fig. 6 to be coupled by the superconductivity matrix element  $\Delta$ . The role of disorder in the superconductor when tunneling to a clean graphene edge has been emphasized recently in Ref. [57].

However, we find that there is a second scenario that leads to a strong proximity effect in the *clean* limit, namely if the interface is transparent. Fig. 7 shows the evolution of the spectrum as the graphene-superconductor hopping matrix element,  $t_{NS}$ , increases. (In order to clearly see the LLL states at  $E = \pm\mu_{\text{gr}}$ , a large value of  $\Delta$  is used,  $\Delta/\mu_{\text{gr}} = 2$ , so that they are not hidden by the superconductor's continuum.) For small  $t_{NS}$  (green line), an avoided crossing appears in the  $K$  valley at  $E = \mu_{\text{gr}}$  where the electron and hole states of the terminated-lattice spectrum cross. The avoided crossing indicates electron-hole hybridization. As  $t_{NS}$  grows, the spectrum changes throughout the Brillouin zone and goes well beyond a simple avoided crossing: one state is pushed to higher energy while the other becomes a CAEM with antisymmetry about the  $K$  point (black). The large hopping matrix element at a transparent interface can couple

many Landau levels,  $t_{NS} \gg E_L$  (in Fig. 7,  $t/E_L = 8$ ), and completely reorganizes the electron and hole states. In this reorganization, the small matrix element of superconductivity readily causes electron-hole hybridization.

We conclude that while a superconductor cannot induce a proximity effect on a clean zigzag QH edge through tunneling—the dead end applies when  $t_{NS} \ll t$ —a strong proximity effect can readily occur when  $t_{NS} \sim t$  so that the interface is transparent. The induced pairing correlations are quite different in these two scenarios. In the first (disorder, tunneling), sublattice-valley locking implies that the graphene sublattice structure of the electrons and holes is the same. In the second scenario (clean, transparent), the electrons and holes are on opposite sublattices, as in Figs. 1(a) and 5.

### C. Spectrum of the CAEM

We now turn to discussing in more detail the energy spectrum of the graphene-superconductor system. Fig. 8 shows an example for each stitching when the superconductor is well-matched and the interface is transparent [89]. In each plot, the BdG spectrum for two values of the superconducting gap are superposed,  $\Delta/E_L = 0.1$  (green) and 0.5 (blue). The smaller value is more realistic, but results for the larger value are instructive because the bulk LLL QH states are within the superconducting gap,  $\Delta > \mu_{\text{gr}} = E_L/4$ , making the figures clearer. With the gauge that we use, the QH states with guiding center coordinate at the interface,  $\bar{y} = 0$ , correspond to  $k = K = 2\pi/3a$  and  $k = K' = 4\pi/3a$ .

For the larger superconducting gap (blue), the energies of the bulk LLL states are clear (horizontal blue lines at  $\pm\mu_{\text{gr}}$ ); they mark the energy of the electron and hole Dirac points. The range of the superconductor's continuum states—the thicket of states at energies  $> \Delta$ —differs for the three cases due to the size of the Fermi surface. It is largest for dense stitching [panel (a)] in which the superconductor's band structure is folded back into the graphene Brillouin zone because the period of the square lattice is  $a/2$ . For the smaller superconducting gap (green), the QH states hybridize with the superconducting continuum and largely disappear as a distinct signature in the spectrum.

Two CAEM are present at the chemical potential near  $k = K$  or  $K'$ , while the two terminated-lattice edge states on the other edge of the nanoribbon are basically unchanged [compare to Fig. 6(c)]. The velocity of the CAEM are substantially reduced compared to those at a terminated-lattice edge, especially for the smaller value of  $\Delta$  (see insets). This velocity reduction results from the slow decay of the wavefunction in the superconductor which implies that the particles spend a substantial amount of time there. The velocity reduction is consistent with the QH rule of thumb [91] that a softer barrier leads to a smaller velocity.

A striking feature of the CAEM dispersion in all three

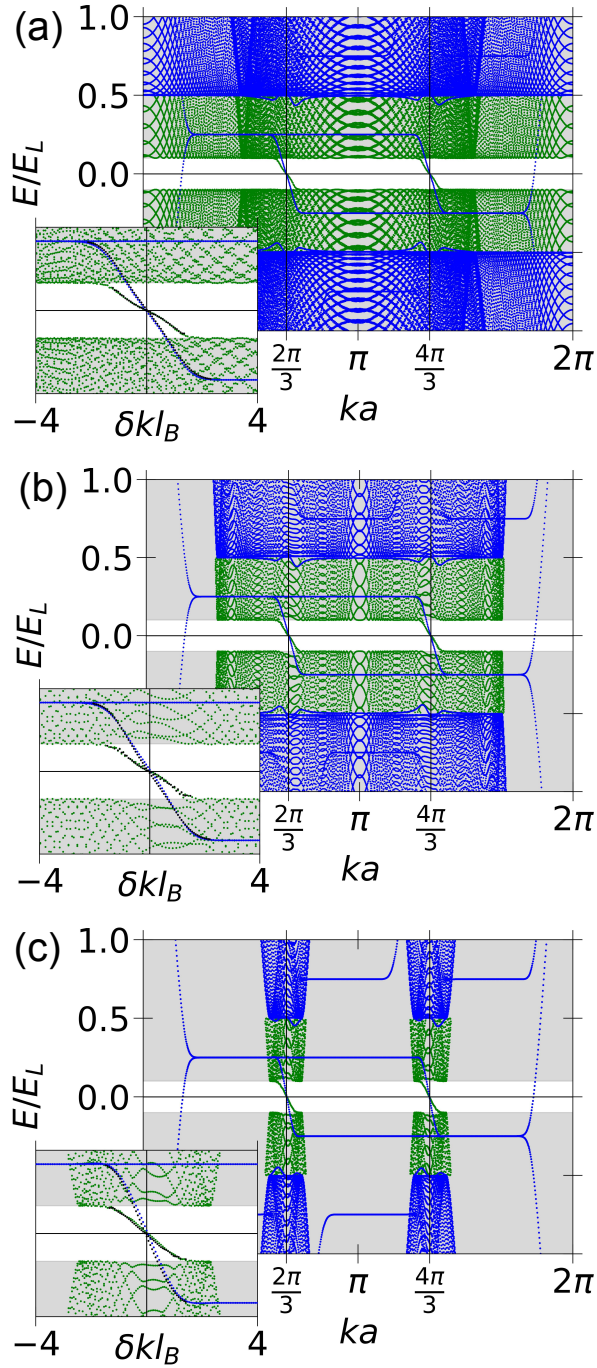


Figure 8. Energy of BdG states (electrons and holes) for interfaces with the three different superconductors—(a) dense square lattice, (b) sparse square lattice, and (c) honeycomb lattice (see Fig. 2)—for two values of the superconducting gap,  $\Delta/E_L = 0.1$  (green) and  $0.5$  (blue). In each case,  $\mu_S$  is chosen so that the superconductor and graphene are well-matched:  $\mu_S/t = 4.5, 5, 0.2$  for dense, sparse, and honeycomb, respectively. For energies above the superconducting gap, the spectrum becomes dense due to the large density of states in the superconductor. Insets: Zoom on the region around the  $K$  point in which  $-E_K(-\delta k)$  is also plotted (black). The fact that the black data nearly perfectly overlay the blue and green demonstrates excellent valley degeneracy. (Standard parameters, Sec. IID.)

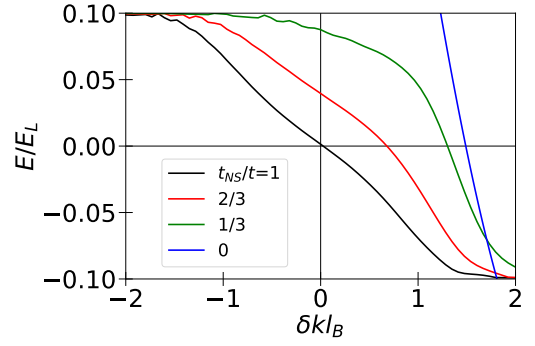


Figure 9. Edge mode dispersion for different strengths of coupling to the superconductor: tight-binding results for small pairing gap,  $\Delta/E_L = 0.1$  ( $\Delta < \mu_{gr}$ ), and zoom on the  $K$  valley. Here,  $E < \Delta$  and  $\delta k \equiv k - K$  is scaled by  $l_B$  [compare to the continuum result in Fig. 1(c)]. The values  $t_{NS}/t \in \{0, 1/3, 2/3, 1\}$  correspond to interface transparency  $\{0, 0.25, 0.7, 0.85\}$ , respectively [87]. The spectrum evolves from the terminated-lattice edge mode (blue) to the fully-hybridized interface mode centered on the  $K$  point (black). (Sparse stitching, otherwise standard parameters, Sec. IID.)

cases is that the  $E = 0$  state is very close to the center of the valley,  $k_0 \approx K$  or  $K'$ . Indeed, the dispersion is *valley degenerate* [77], by which we mean

$$E_K(\delta k) = E_{K'}(\delta k) \quad (22)$$

where  $\delta k$  is the deviation from the corresponding valley center. Combining this with the particle-hole symmetry relation for a spin-independent BdG equation,  $E_K(\delta k) = -E_{K'}(-\delta k)$ , one finds that the dispersion is antisymmetric within each valley,

$$E_K(\delta k) = -E_K(-\delta k). \quad (23)$$

The excellent antisymmetry shown in the insets thus demonstrates nearly perfect valley degeneracy.

Furthermore, we find that a valley degenerate spectrum *requires* a transparent, well-matched interface. The breaking of valley degeneracy is readily seen by placing a barrier at the interface (the effect of changing  $\mu_S$  is discussed in the next section). In the tight-binding model, the hopping at the interface,  $t_{NS}$ , is reduced, and we presented above in Fig. 7 results for the larger value of  $\Delta$ . In the continuum model, the parameter controlling the transparency of the interface is the strength of the  $\delta$ -function potential at the interface,  $V_0$ , which affects the boundary condition Eq. (14) by effectively increasing the imaginary part of  $q$  (see App. D for details).

Figs. 9 and 1(c) show tight-binding and continuum results, respectively, for the CAEM dispersion in the  $K$  valley for the smaller value of the gap,  $\Delta = 0.1E_L$ . The avoided crossing for small  $t_{NS}$  is less clear than in Fig. 7 because of hybridization with the continuum of states in the superconductor for  $E > \Delta$ . Nevertheless, in both the tight-binding and continuum results, there is a similar evolution from the QH edge state to an antisymmetric dispersion about the center of the valley. We note an interesting change in the curvature of the dispersion in

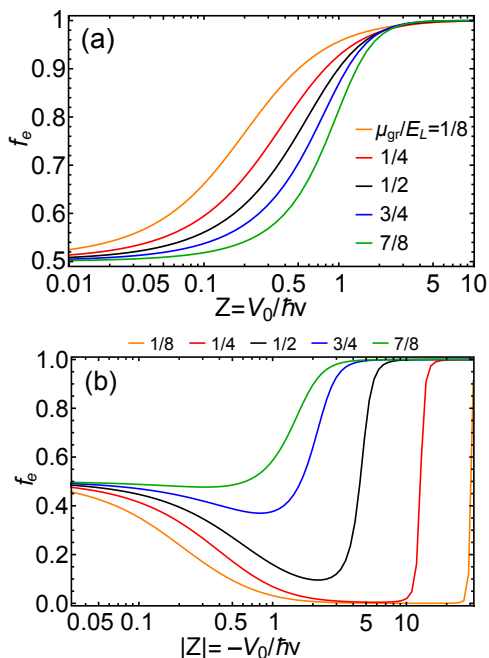


Figure 10. Fractional electron content in graphene [ $e$ - $h$  hybridization, Eq. (1)] as a function of the strength of (a) a barrier or (b) a potential well at the interface. Continuum model results are shown, varying the filling,  $\mu_{\text{gr}}/E_L$ , of the CAEM. (Standard parameters, Sec. IID.)

both the tight-binding and continuum results: for a low transparency interface, the curvature is negative near the  $K$  point, while for full-transparency, there is an inflection point at  $\delta k = 0$  and the curvature is positive for  $\delta k < 0$ .

In these zooms on the  $K$  valley, the decrease in velocity of the CAEM as transparency increases is particularly clear. We discuss this further in App. D 3 for the continuum model, giving an analytic expression. Over an interval  $\delta k$  of order  $1/l_B$ , the energy changes by  $\sim E_L$  for a QH edge state but only by  $\sim \Delta$  for a CAEM.

Hand in hand with these changes in the CAEM dispersion, the presence of a barrier changes the electron-hole hybridization of the state at the chemical potential. Fig. 10 shows the hybridization as a function of the barrier strength in the continuum model, for the case of perfect hybridization when  $Z = 0$  ( $\tilde{v}^2 = 1$ ). The presence of a barrier at the interface prevents contact with the superconductor and thus drives the  $K$ -valley mode toward being fully electron-like [panel (a)]. The effect of the barrier is more pronounced for lower filling where the particles have less kinetic energy. On the other hand, panel (b) shows that a potential well at the interface,  $Z < 0$  with  $|Z| \sim 1$ , can enhance the hole content.

#### D. Valley Degeneracy, Interface Transparency, and Andreev Reflection

Valley degeneracy is *not* accidental but rather is a universal feature of well-hybridized states [77]. Moreover, valley degeneracy is *independent* of the graphene chem-

ical potential (for  $\mu_{\text{gr}}$  not too close to the Dirac point): the interface mode “self-aligns” so that  $E_K(\delta k = 0) = 0$  throughout the LLL. We find that this holds for *all* of the well-matched, highly transparent tight-binding and continuum cases that we have studied.

There is a natural connection between strong Andreev reflection, good interface transparency, and valley degeneracy. Since  $e$ - $h$  conversion can occur only in the superconductor, an incoming electron should interact with the superconductor as much as possible. A transparent interface ensures that any ingoing electron component from the graphene comes out as a hole (not as a scattered electron). Furthermore, since the electron and hole components in the superconductor have equal weight at  $E = 0$ , so should the two components in graphene in order to achieve good wavefunction matching at the interface. In fact, the two components should have the same spatial profile (as a function of  $y$ ): a Fourier decomposition of the incoming electron leads to a hole emerging with the same Fourier decomposition (up to phases) and so the same shape. Thus, for strong Andreev reflection, the guiding center coordinate of the electron and hole components of the  $E = 0$  state must be similar.

On the other hand, the wavevector along the interface of the electron and hole components must be equal. But for electrons and holes the relation between the guiding center and the wavevector is opposite:  $\text{sign}(\delta \bar{y}) = -\text{sign}(\delta k)$  for electrons but  $\text{sign}(\delta \bar{y}) = +\text{sign}(\delta k)$  for holes (with our sign conventions). To have the same guiding center *and* wavevector requires, then,  $\delta \bar{y} = \delta k = 0$ .

In the LLL of the terminated lattice spectrum, Fig. 6, such a state exists only for the fine-tuned case  $\mu_{\text{gr}} = E_L$  [78, 84]. In contrast, for a transparent interface,  $t_{NS} \sim t \gg E_L \gg \Delta$ , an approximately Gaussian wavefunction centered at  $\delta \bar{y}_0 = 0$  can be constructed, by mixing in small amplitudes of higher Landau level edge states. Alternatively, using the bulk QH complete basis, a small modification of the LLL wavefunction at  $\delta \bar{y} = \delta k = 0$  shifts its energy from the Dirac point to the chemical potential. *Thus, we see that for a transparent interface a “self-aligned”  $E = 0$  interface mode, i.e.  $\delta \bar{y}_0 = \delta k_0 = 0$  with no tuning, is natural.*

This self-aligned interface mode is evident in the tight-binding numerics, Figs. 5, 8, and 9, as well as the continuum results, Fig. 1. Once  $E(\delta k = 0) = 0$  is established, full valley degeneracy follows in two steps. First, the spectrum within a given valley should be antisymmetric in  $\delta k$  because the role of electrons and holes is exactly conjugate for a transparent interface. Second, the BdG particle-hole symmetry then implies valley degeneracy.

The general argument given above manifests itself clearly in the equations for the continuum solution in App. D. Perfect hybridization means  $|C_1| = |C_2|$  [see Eq. (A12)]. Since the ratio of these two coefficients, given in Eq. (D9), depends on the ratio of closely related parabolic cylinder functions evaluated at  $y = 0$ , one can readily deduce that  $|C_1/C_2| = 1$  at  $E = 0$  implies  $\delta \bar{y}_0 = \delta k_0 = 0$  independent of  $\mu_{\text{gr}}$ : this is the self-aligned CAEM. The

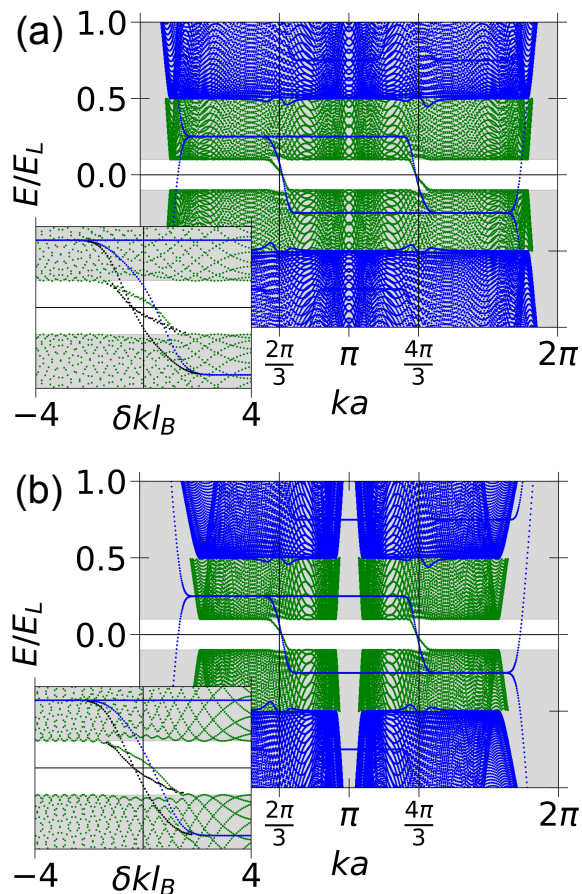


Figure 11. Energy of BdG states for larger Fermi surface in the superconductor: (a) sparse square lattice with  $\mu_S/t = 4.2$  and (b) honeycomb lattice with  $\mu_S/t = 0.8$ . Spectra for two values of the superconducting gap are superposed,  $\Delta/E_L = 1/10$  (green) and  $1/2$  (blue). Insets: Zoom on the region around the  $K$  point in which  $-E_K(-\delta k)$  is also plotted (black). The black data do not overlay the blue and green—the deviation of  $k_0$  from the valley center is given in Table I—demonstrating that valley degeneracy is broken. (Parameters otherwise standard, Sec. IID.)

secular equation then gives full valley degeneracy.

## V. VARY FERMI ENERGY OF SUPERCONDUCTOR

In this section, we return to an issue mentioned briefly above: how the electron-hole hybridization is influenced by the superconductor's Fermi energy.

### 1. Tight-binding model

In the tight-binding model, suppose we make the size of the Fermi surface larger and so more metallic-like. For the honeycomb lattice, we increase  $\mu_S$  substantially, and for the sparse square lattice, we bring  $\mu_S$  closer to the middle of the band. Since the dense square lattice has a

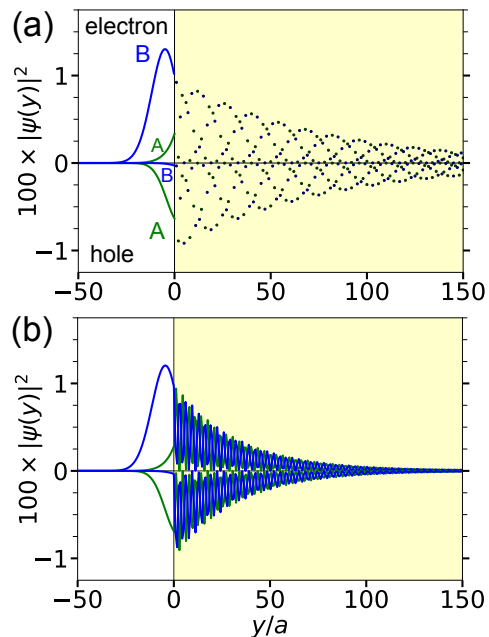


Figure 12. Mode wavefunctions  $|\psi(y)|^2$  of the  $E=0$  state in the  $K$  valley for the spectra in Fig. 11: (a) sparse square lattice with  $\mu_S=4.2t$  and (b) honeycomb lattice with  $\mu_S=0.8t$  ( $\Delta/E_L = 1/10$ ). The degree of  $e$ - $h$  hybridization is given in Table I. The wavefunction has the same qualitative structure as in the well-matched cases (Fig. 5), but the hole content is substantially smaller than the electron content. (Parameters otherwise standard, Sec. IID.)

Fermi surface that covers the entire Brillouin zone (due to folding), we do not consider it for this comparison. The resulting spectra are shown in Fig. 11 and wavefunctions in Fig. 12. By comparing the widths of the superconductor continuum to those in Fig. 8, one can see the extent to which the Fermi surface has been enlarged.

The spectra here are qualitatively similar to each other but distinctly different from the optimal case (Fig. 8) in that valley degeneracy is absent. Valley degeneracy implies antisymmetry, Eqs. (22)-(23), and the black lines in the insets [which are  $-E_K(-\delta k)$ ] clearly do not overlay the blue and green. Quantitatively, the deviation of the  $E=0$  state from  $K$ ,  $\delta k_0$ , is given in Table I for both cases: though much larger than for the well-matched cases, these values are still smaller than for the QH terminated-lattice edge state [92]. Because  $\delta k_0$  is of order  $1/l_B$ , the guiding center coordinates of the electron and hole components differ by of order  $l_B$ , and thus their spatial profiles differ substantially.

The differing spatial profiles are clear in the wavefunctions in Fig. 12. On the QH side, the electron weight is considerably larger than the hole weight—quantitatively, see Table I for the values of  $f_e$ . The form of the electron component on the B sublattice continues to be truncated bulk-like. On the superconductor side, the wavefunction is no longer as simple as in Fig. 5: the rapid oscillations due to the large  $k_{FS}$  are out of phase with the lattice.

Importantly, in order to achieve good electron-hole hybridization,  $\mu_S$  does *not* have to be very carefully chosen.

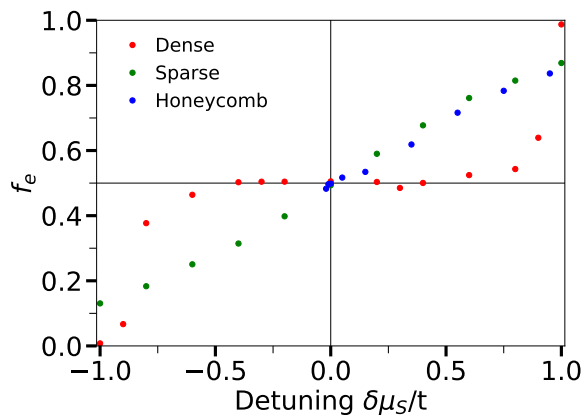


Figure 13. Fractional electron content in graphene [ $e$ - $h$  hybridization, Eq. (1)] as a function of the chemical potential of the superconductor for the three tight-binding stitchings (Fig. 2). Detuning is from the optimal value (see Sec. IID; parameters otherwise standard). Note the especially wide window of excellent hybridization in the dense case (red).

Fig. 13 shows how the hybridization changes upon detuning  $\mu_S$  from the optimal value. As a rough criterion for good hybridization, we use  $|f_e - \frac{1}{2}| \lesssim 0.1$ . The wavefunction at the chemical potential satisfies this criterion for  $\mu_S \in [3.3, 4.8]t$  for dense stitching,  $\mu_S \in [4.8, 5.2]t$  for sparse stitching, and  $\mu_S \in [0, 0.4]t$  for the honeycomb lattice. For both square lattice cases, the regime of good matching (strong coupling) occurs when the Fermi energy of the superconductor is much larger than that of graphene, suggesting that graphene is particularly suitable for interfaces to superconductors.

Dense stitching, which is especially attractive since the Fermi surface is large, yields good  $e$ - $h$  hybridization for about one fifth of the total band width of the superconductor—a very substantial range. Because in the experimental systems the superconductor likely connects to both sublattices of graphene and has several Fermi surface sheets, we expect the dense stitching results to be the most relevant.

We find that the degree of hybridization depends only weakly on graphene doping,  $\mu_{gr}/E_L$ , in all of these cases (not shown). Thus, if the superconductor is well matched to graphene (i.e. with  $\mu_S$  in the optimal range) then, as in the continuum model Fig. 1(b), there is good electron-hole hybridization throughout the LLL.

## 2. Continuum model

How the hybridization changes with  $\mu_S$  for the continuum model is shown in Fig. 14. As the Fermi energy of the superconductor deviates from its optimal value,  $\tilde{v}^2 \leq 1$ , the CAEM has more electron or hole character. For low graphene filling, the insensitivity of the hybridization to the superconductor's properties stands out.

Even for a large variation in the properties of the superconductor, Fig. 1(b) shows that the hybridization remains good throughout the LLL. The underlying rea-

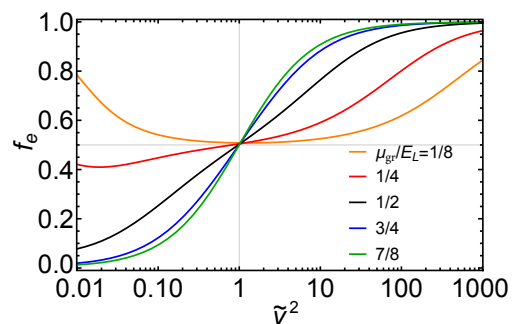


Figure 14. Fractional electron content in graphene as a function of imperfect matching due to the superconductor chemical potential (no barrier,  $Z=0$ ). Continuum model results shown for different CAEM filling  $\mu_{gr}/E_L$ .  $\tilde{v}^2$  is defined in Eqs. (15)-(16). (Parameters otherwise standard, Sec. IID.)

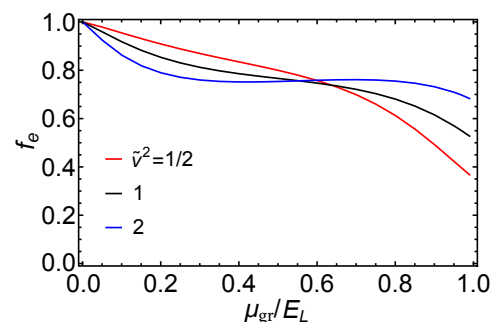


Figure 15. Fractional electron content in graphene as a function of the filling of the LLL interface mode for an imperfect interface. Shown for three values of the superconductor Fermi energy,  $\tilde{v}^2=1/2, 1, 2$ , in the continuum model with the interface barrier strength set to  $Z = V_0/\hbar v = 0.5$ . (Parameters otherwise standard, Sec. IID.)

son is that current continuity involves the velocity at the Dirac point, which is insensitive to external parameters. For instance, for a given superconductor, the velocity  $\hbar K/m$  is fixed with respect to the Dirac point velocity. For  $\hbar K/m = 2v$ , varying  $\tilde{v}^2$  from  $1/2$  to  $2$  [as in Fig. 1(b)] corresponds to changing the Fermi energy of the superconductor by a factor of 2, while for  $\hbar K/m \ll v$ , such a variation changes  $\mu_S$  by a factor of 4. Only the unlikely case  $\hbar K/m \approx v$  leads to undesirable rapid variability. Thus, in contrast to the usual semiconductor case [43, 45, 57, 58, 81], no fine-tuning is needed to have excellent Andreev reflection in graphene in the QH regime.

Finally, we present in Fig. 15 results when both a detuned  $\mu_S$  and a small interface barrier,  $Z = 0.5$ , are present. There continues to be only a modest dependence on the Fermi surface of the superconductor through  $\tilde{v}^2$ , but there is somewhat more dependence on the graphene chemical potential  $\mu_{gr}$ . Note, however, that the dependence is smooth: there continues to be no indication that fine-tuning is needed to obtain strong Andreev reflection.

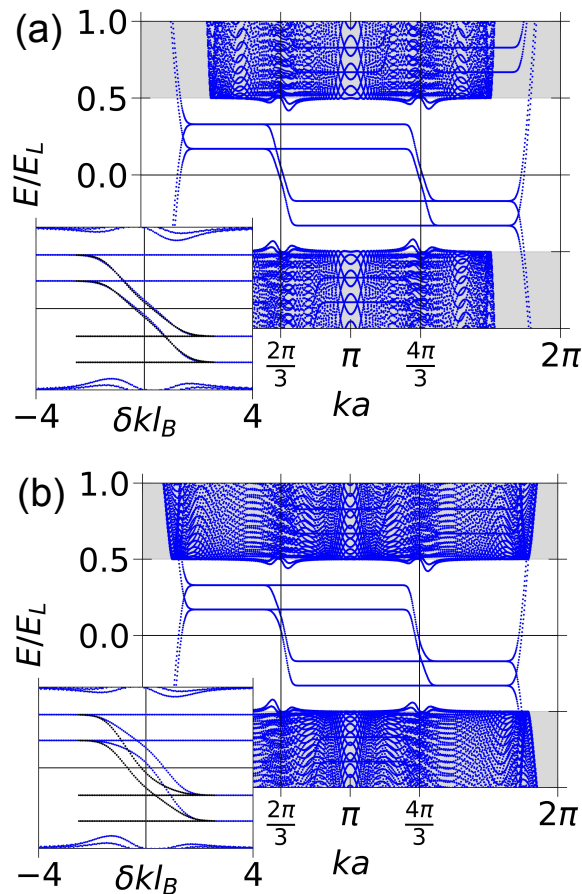


Figure 16. Energy of BdG states for sparse stitching with Zeeman splitting: (a) well-matched, transparent interface ( $\mu_S/t=5$ ) and (b) imperfect ( $\mu_S/t=4.2$ ). Insets: Zoom on the region around the  $K$  point in which the  $K'$ -valley spectrum,  $E_{K'}(\delta k)$ , is also plotted (black). The deviation of  $k_0$  from the valley center is given in Table II. Valley-degeneracy is very good for the transparent interface (though the dispersion is not antisymmetric about  $\delta k=0$ ) but broken for a non-ideal interface. ( $\Delta/E_L=0.5$ ; parameters otherwise standard, Sec. II D.)

## VI. SPIN: ZEEMAN-SPLIT MODES

We now present results in which the Zeeman effect is included (spin-orbit coupling is still not included). The magnetic field in graphene acts on the spin of the electron and splits the spin up and down solutions, leading to two modes in each valley [93]. The modes in the  $K$  valley are, of course, related to those in the  $K'$  valley by the BdG particle-hole symmetry:  $E_{K\uparrow}(\delta k) = -E_{K'\downarrow}(-\delta k)$ .

The spectrum for tight-binding with sparse stitching is shown in Fig. 16(a) for a well-matched case. The Zeeman splitting is  $\Delta_z = E_L/6$  (corresponding to a large g-factor for illustration). The bulk LLL is split in two (horizontal lines), and a CAEM connects the higher energy electron line to the higher energy hole line [compare to Fig. 8(b) for zero Zeeman effect].

Importantly, note that the spectrum remains *valley degenerate*: the inset highlights  $E_{K\uparrow}(\delta k) = E_{K'\uparrow}(\delta k)$ .

Fig. (panel)	Fractional electron content, $f_e$	Deviation from valley center, $\delta k_0 l_B$
17(a)	0.34	-0.28 [unsplit: 0.01]
17(b)	0.68	0.36
18(a)	0.72	0.17 [unsplit: 0.42]
18(b)	0.89	0.70

Table II. For the Zeeman-split tight-binding wave functions in Figs. 17 and 18, we give the fractional electron content in graphene and the deviation of the wavevector  $k_0$  for the  $E=0$  mode from the center of the  $K$  valley:  $\delta k_0 l_B \equiv (k_0 - K)l_B$ .

However, because of the spin index, particle-hole symmetry plus valley degeneracy no longer imply that the dispersion is antisymmetric within a valley,  $E_{K\uparrow}(\delta k) \neq -E_{K\uparrow}(-\delta k)$ . Thus, the zero energy excitations need not occur at the valley centers. In fact, the two solutions are shifted oppositely from the valley center—the values of  $\delta k_0$  are given in Table II, together with those for no Zeeman effect (labeled unsplit). Though additional momentum differences among the  $E=0$  modes are thus generated by Zeeman splitting, no new interference effects can occur in transport since the up and down spin modes are completely uncoupled.

For an imperfectly matched interface, the spectrum is shown in Fig. 16(b). The spectrum now is definitely *not* valley degenerate, just as in the absence of Zeeman splitting (Fig. 11): the difference in the  $K$  and  $K'$  valley spectra is seen clearly in the inset. As in the transparent interface (see Table I), the two modes shift oppositely from the zero-Zeeman case, but now both modes occur on the same side of the valley center—both  $\delta k_0$  are positive in the  $K$  valley and negative in  $K'$  (see Table II). Since the modes that can interfere now have different  $\delta k_0$ , new interference effects are possible.

Our results for a well-matched, transparent interface are quite different from those in a recent paper, Ref. [62]. There, the authors emphasize that in breaking the  $SU(4)$  symmetry of the problem, a Zeeman field produces modes with different group velocities. We see here that this is not the case for a transparent interface. Rather, for a transparent interface, the spectrum remains valley degenerate despite the Zeeman field, and the velocities of all four modes are the same. On the other hand, our results for an imperfect, poorly matched interface are in agreement with those of Ref. [62].

Ref. [62] makes an interesting comment on the possibility of achieving Majorana modes when the canted antiferromagnet state of the LLL [12, 94, 95] is coupled to a superconductor. The authors point out that the induced gap that supports Majorana modes vanishes if  $\delta k_0$  is too large, and therefore suggest that the observability of such modes may be overstated in the literature. However, this conclusion was reached by considering an interface with poor transparency. Here, we point out that for a well-matched, transparent interface, one finds  $\delta k_0 l_B \ll 1$  in the absence of Zeeman splitting, and even with Zeeman splitting,  $\delta k_0 l_B$  is not large. Thus, the more optimistic sce-

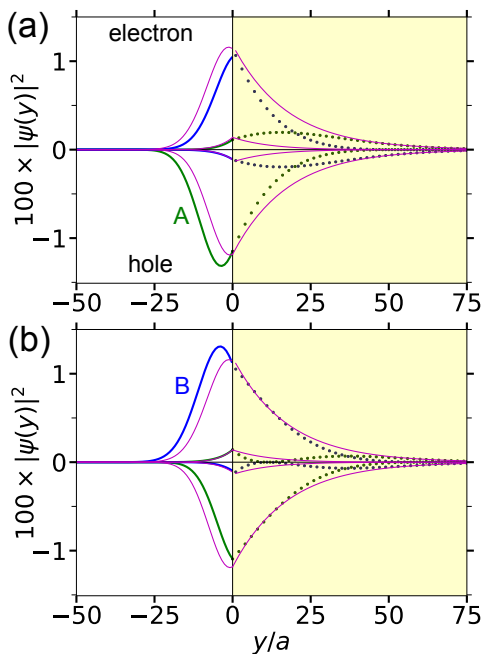


Figure 17. Wavefunctions,  $|\psi(y)|^2$ , for the two Zeeman-split modes in the  $K$  valley at the chemical potential ( $E = 0$ ): (a) spin up and (b) spin down solutions. The sparse-stitching interface is well matched and so maximally transparent. The degree of  $e$ - $h$  hybridization is given in Table II. The magenta line is the zero-Zeeman case for comparison. (Correspond to spectrum in Fig. 16(a).)

nario for achieving Majorana modes appears to be possible as long as the graphene-superconductor interface is transparent.

Turning to the corresponding wavefunctions for  $E = 0$ , we see in Fig. 17 that for a transparent interface the electron-hole balance has been disrupted. Specifically, on the graphene side the main parts of the electron and the hole components, which correspond to the bulk states, displace oppositely relative to the interface, as expected for  $\delta k_0 \neq 0$  (see Sec. IV D). In one mode the electron component shifts toward the interface and gets smaller and the hole component shifts away and gets bigger, while the reverse occurs in the other mode. In contrast, the small, exponentially decaying surface components are not modified. In the superconductor, the wavefunction continues to have a clear even-odd and electron-hole alternation, though the form is modified.

For an imperfectly matched interface, the wavefunctions are shown in Fig. 18. The effect of the Zeeman field is similar to the transparent case (again the exponentially decaying surface components are barely affected). Note that for the mode in panel (a), because the imperfect interface by itself produces  $e$ - $h$  unbalanced modes, the Zeeman effect actually brings the electron and hole closer spatially and makes their weights more similar. [The opposite is true for the other mode, panel (b).] Thus, under the symmetry breaking connected with the Zeeman effect, Andreev reflection can become *stronger*.

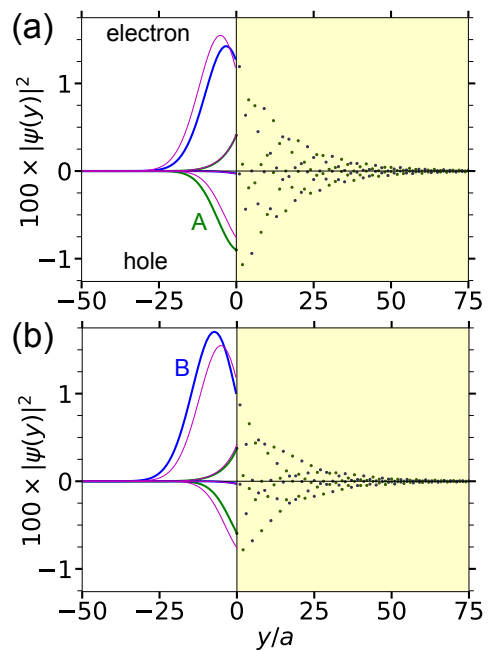


Figure 18. For an imperfect interface, wavefunctions for the two  $E = 0$  modes in the  $K$  valley as they are split by the Zeeman effect: (a) spin up and (b) spin down solutions. Here,  $\mu_S/t = 4.2$ . The magenta line is the zero-Zeeman case for comparison (not plotted in superconductor for clarity). (Correspond to spectrum in Fig. 16(b).)

## VII. CONCLUSIONS

We have presented results for an infinite graphene/superconductor interface using continuum and tight-binding models in the standard mean-field approach to spatially inhomogeneous superconductivity (BdG equation). Our main assumptions are: (i) disorder is absent and (ii) the fields  $\Delta$ ,  $B$ , and  $U$  are taken to be step functions at the interface. The continuum results are particularly helpful in exploring a wide range of parameters.

The primary conclusion is that strong Andreev reflection, and hence strong electron-hole hybridization, is much easier to achieve with graphene than with a typical semiconductor 2D electron gas. The reason is that the velocity at the Dirac points in graphene is large—of order the Fermi velocity of metals—and independent of the graphene chemical potential or density. Thus, current continuity across the interface can be satisfied without a great deal of electron reflection.

In order to actually realize strong Andreev reflection, the interface should be fairly transparent. In particular, there should be no obvious barrier, and the superconductor should be well-matched, having Fermi level states with wavevector larger than  $K$  and velocity of order  $v$  (corresponding to the wave vector of the Dirac point and the Fermi velocity of graphene). This does not appear to be a stringent restriction, since the Fermi surface of metals used for thin-film superconductors often have several sheets, allowing for several possible matches.

Previous work has emphasized that fine-tuning is nec-

essary in order to achieve electron-hole hybridization at a clean QH/superconductor interface [45, 57, 58]; for instance, the chemical potential in the QH material should be tuned on an energy scale less than  $E_L$ . We emphasize that this is *not* the case for graphene. Once one obtains a fairly well-matched, transparent interface, which may involve “coarse-tuning” the choice of superconductor on an energy scale of the bandwidth ( $\gg E_L$ ), the  $e$ - $h$  hybridization in a graphene CAEM is ideal and independent of filling. Indeed, the dispersion of the CAEM self-aligns to be antisymmetric within each valley, independent of filling. Thus, the spectrum is valley degenerate, and the guiding center coordinate of the state at the chemical potential is at the graphene/superconductor interface.

The CAEM wavefunction in graphene exhibits particularly simple structure in the case of a well-matched interface. The hole component is nearly the same as the electron but with the sublattices interchanged. This pairing of two electrons on *different* sublattices is distinctly different from that induced by tunnel-coupling to a disordered superconductor in which two electrons on the *same* sublattice are paired.

In the spatial profile of the wavefunction, the weight of the electron component is primarily on the sublattice corresponding to the bulk LLL state (sublattice-valley locking), and is surprisingly close to a truncated bulk wavefunction. This demonstrates that the terminated-lattice QH edge states are a poor starting point for understanding the CAEM of a transparent interface, an unsurprising result in hindsight in view of the very different boundary conditions.

In future work, the role of disorder, both in the superconductor and along the interface, should be further developed in the context of a transparent graphene/superconductor interface (for initial work see Ref. [53] and for the importance of disorder in the tunneling regime see Ref. [57]). We suspect that disorder will decrease the dependence on  $\mu_S$  in our models and so increase the window of good electron-hole hybridization. A second clear direction is to include the penetration of the magnetic field into the superconductor in the form of vortices. It is likely that tunneling of electrons into states in the vortices is an important source of loss in the experiments [29, 30], and theoretical work assessing the importance of this effect has recently appeared [55, 60, 63]. Third, the role of spin-orbit coupling should be investigated. While such coupling is weak in graphene, in several of the superconductors typically used it is strong. Finally, perhaps the most straight forward extension of our results is to the properties of nanostructures, which involves scattering between these CAEM at junctions, corners, and quantum point contacts.

## ACKNOWLEDGMENTS

We thank Anthony David, Gleb Finkelstein, William Klein, and Lingfei Zhao for helpful discussions. The work

in the USA was supported in part by the U.S. Department of Energy, Office of Science, Office of Basic Energy Sciences, Materials Sciences and Engineering Division, under Award No. DE-SC0005237. A.B. acknowledges support by the 2019 Department of Defense NDSEG fellowship. G.Z. acknowledges support from the National Natural Science Foundation of China (Grant No. 12374158) and the Innovation Program for Quantum Science and Technology (Grant No. 2021ZD0302400).

The data that support the findings of this article are openly available [96].

## Appendix A: Specifics of the Models: Tight-Binding and Continuum

In this appendix, we specify the tight-binding and continuum models presented in Sec. II.

In the *tight-binding model*, the normal state spin-projected hamiltonian of the superconductor is a square lattice in the  $y > 0$  half-plane,

$$H_S(x, y > 0) = -t \sum_{\langle ij \rangle} (|i\rangle\langle j| + \text{h.c.}) - (\mu_S - 4t) \sum_i |i\rangle\langle i|, \quad (\text{A1})$$

where  $\langle ij \rangle$  denotes nearest-neighbor sites.  $\mu_S$  is the chemical potential (Fermi energy) measured from the bottom of the band. Pairing in the superconductor connects the electron and hole states with the same spin [93],

$$\Delta(x, y > 0) = \Delta \sum_i (|i\rangle_e \langle i|_h + \text{h.c.}). \quad (\text{A2})$$

In the absence of spin-orbit coupling and the Zeeman effect, the problem decouples into two independent, identical problems, leading to doubly degenerate states. We therefore focus on the spin-projected system. For Zeeman splitting in Sec. VI, the two problems are still independent (but not identical), and the spin index can easily be introduced.

Graphene is modeled by hopping on a honeycomb lattice with phase factors due to the magnetic field:

$$H_{QH}(x, y \leq 0) = -t \sum_{\langle ij \rangle} \left( e^{-2\pi i \Phi_{ij} / \Phi_0} |i\rangle\langle j| + \text{h.c.} \right) - \mu_{\text{gr}} \sum_i |i\rangle\langle i|, \quad (\text{A3})$$

where  $\Phi_{ij} = \int_{\mathbf{r}_j}^{\mathbf{r}_i} \mathbf{A} \cdot d\mathbf{l}$  and  $\Phi_0 = h/e$  is the flux quantum. We take  $\mathbf{A}(x, y) = By\hat{x}\theta(-y)$ , and with this choice  $\Delta$  in Eq. (A2) is constant and real.  $\mu_{\text{gr}}$  is the chemical potential (Fermi energy) measured from the Dirac point. The terminal row of the zigzag edge is at  $y = 0$  and part of the A sublattice. The graphene half-sheet has period  $a$  in the  $x$  direction (next-nearest-neighbor distance).

To specify the hopping hamiltonian connecting the graphene and superconductor lattices, we use  $a$  as the unit

of length in writing coordinates for a position space basis  $|x, y\rangle$ . For “dense” stitching [Fig. 2(a)], we have

$$\begin{aligned} H_{T,\text{dense}} &= H_T^{(A)} + H_T^{(B)} \\ &\equiv -t_{NS} \sum_n^{(A)} [ |n, \frac{1}{2}\rangle \langle n, 0| + \text{h.c.} ] \\ &\quad - t_{NS} \sum_n^{(B)} [ |n + \frac{1}{2}, \frac{1}{2}\rangle \langle n + \frac{1}{2}, -\frac{\sqrt{3}}{2}| + \text{h.c.} ], \end{aligned} \quad (\text{A4})$$

where the first term connects the square lattice and the terminal A sites of graphene and the second term connects the neighboring B sites directly to the square lattice. Second, in the “sparse” stitching scenario [Fig. 2(b)], the square lattice has the same period as the zigzag edge and only the terminal A sites are connected to the square lattice,

$$H_{T,\text{sparse}} = H_T^{(A)}. \quad (\text{A5})$$

Third, in the “honeycomb” scenario, the graphene lattice is simply continued into the superconductor [Fig. 2(c)].

After constructing the Hamiltonian using the Kwant package [97], we solve for the band structure by Fourier transforming along the  $x$ -direction, using the quasi-1D unit cell of a nanoribbon with width defined by  $-y_{QH} < y < y_S$  [80]. The fractional electron content in graphene is given in terms of the wavefunction by

$$f_e \equiv \frac{\sum_{i \in \text{gr}} |\psi_i^e|^2}{\sum_{i \in \text{gr}} |\psi_i^e|^2 + |\psi_i^h|^2} \quad (\text{A6})$$

where the sum is over all graphene sites (both A and B).

In the *continuum model*, the wavefunction in the superconductor is a solution to the BdG equation with  $H_S$  and  $\Delta$  in Eqs. (5)-(6) and has the Nambu spinor form

$$\begin{aligned} \Psi_S(x, y > 0) &= e^{ipx} \left\{ C_3 \Psi_{S,p}^+(y) + C_4 \Psi_{S,p}^-(y) \right\} \\ &\equiv e^{ipx} \begin{pmatrix} \psi_{S,p}^e(y) \\ \psi_{S,p}^h(y) \end{pmatrix} \end{aligned} \quad (\text{A7})$$

$$\text{with } \Psi_{S,p}^+(y) = \sqrt{q'} e^{iqy} \begin{pmatrix} 1 \\ \gamma \end{pmatrix} \quad (\text{A8})$$

and  $\Psi_{S,p}^-(y) = [\Psi_{S,p}^+(y)]^*$  (with  $\pm$  indicating the direction of evanescent current perpendicular to the interface) [68]. For  $E < \Delta$ ,  $q$  and  $\gamma$  are given by

$$\gamma = \frac{E - i\sqrt{\Delta^2 - E^2}}{\Delta}, \quad (\text{A9})$$

$$q^2 = (k_{FS}^2 - p^2) + i \frac{2m}{\hbar^2} \sqrt{\Delta^2 - E^2}. \quad (\text{A10})$$

Note that  $|\gamma| = 1$ , implying an equal weight of electrons and holes in the superconductor. For the  $E = 0$  states,  $\gamma = -i$  and  $q^2$  simplifies as in Eqs. (8) and (16).

On the graphene side, the wavefunction is proportional to  $e^{ikx}$ , and because of translational invariance,

the amplitudes for the  $K$  and  $K'$  valleys are independent, Eq. (11). In terms of spinors in both sublattice and  $e$ - $h$  indices, the solution in valley  $K$  is of the form

$$\Psi_K(x, y < 0) \equiv e^{ikx} \Psi_{K,k}(y), \quad (\text{A11})$$

$$\Psi_{K,k}(y) \equiv C_1 \begin{pmatrix} \phi_{1k}^e(y) \\ \phi_{2k}^e(y) \end{pmatrix} \otimes \begin{pmatrix} 1 \\ 0 \end{pmatrix} + C_2 \begin{pmatrix} \phi_{1k}^h(y) \\ \phi_{2k}^h(y) \end{pmatrix} \otimes \begin{pmatrix} 0 \\ 1 \end{pmatrix}, \quad (\text{A12})$$

with two undetermined coefficients. The transverse wavefunctions appearing in the boundary conditions Eqs. (12)-(13) are, for example,  $\psi_{KA,k}^e(y) = C_1 \phi_{1k}^e(y)$  and  $\psi_{KB,k}^h = C_2 \phi_{2k}^h(y)$ . For the  $K'$  valley, the form of the transverse wavefunction is given by a simple interchange of the sublattices:  $\Psi_{K',k}(y) = -i\sigma_y \Psi_{K,k}(y)$ .

In the absence of a magnetic field, the transverse wavefunctions are plane waves. An ingoing electron is reflected as either an electron or a hole (see App. C).

In the QH regime, the transverse solutions  $\phi_{n,k}^\beta(y)$  are parabolic cylinder functions [43, 77, 78]. We normalize them to unity,

$$\int_{-\infty}^0 dy \{ |\phi_{1k}^\beta(y)|^2 + |\phi_{2k}^\beta(y)|^2 \} = 1, \quad (\text{A13})$$

and write them explicitly in Appendix D. In addition, we normalize the full transverse wavefunction to unity

$$1 = \sum_{i=1}^4 |C_i|^2 = |C_1|^2 + |C_2|^2 + 2|C_4|^2. \quad (\text{A14})$$

The four unknowns in the wavefunction—the  $\{C_i\}$  in Eqs. (A7) and (A12)—are determined by the boundary conditions (12)-(13) together with the normalization conditions. Thus, the energies and wavefunctions of the interface modes are found. In terms of the wavefunction (A12), the fractional electron content in graphene is

$$f_e \equiv \frac{|C_1|^2}{|C_1|^2 + |C_2|^2}. \quad (\text{A15})$$

## Appendix B: Boundary Condition in the Continuum Model

In this appendix we derive the current continuity boundary condition between graphene and a superconductor with parabolic dispersion, within the continuum model. We match the expectation value of the particle current (not the charge current). Since electrons cannot be instantaneously converted into holes, the current of electrons and holes must each match.

The expectation value of the particle current is conveniently written in terms of the components of the Nambu spinor. In the superconductor, in terms of the components defined in Eq. (A7), the current perpendicular to

the interface is

$$j_S^e = \frac{i\hbar}{2m} (\psi_S^e \partial \psi_S^{e*} - \psi_S^{e*} \partial \psi_S^e), \quad (\text{B1a})$$

$$j_S^h = -\frac{i\hbar}{2m} (\psi_S^h \partial \psi_S^{h*} - \psi_S^{h*} \partial \psi_S^h), \quad (\text{B1b})$$

for electrons and holes, respectively. In graphene, the electron and hole currents in valley  $K$  perpendicular to the interface are [77]

$$j_{K\text{gr}}^e = v (\psi_{KA}^{e*} \psi_{KB}^e + \psi_{KB}^{e*} \psi_{KA}^e) \quad (\text{B2a})$$

$$j_{K\text{gr}}^h = -v (\psi_{KB}^{h*} \psi_{KA}^h + \psi_{KA}^{h*} \psi_{KB}^h). \quad (\text{B2b})$$

The corresponding expressions in the  $K'$  valley [77] have a minus sign. Note that the current in graphene does not involve the derivative of the wavefunction but rather the amplitudes on the A and B sites, which are nearest neighbors in the honeycomb lattice.

There are four cases to consider ( $e$  and  $h$  in valleys  $K$  and  $K'$ ); as an example, we consider the case of electrons in valley  $K$ . Setting the current on the two sides of the interface equal yields

$$\begin{aligned} 0 &= j_S^e - j_{K\text{gr}}^e \quad (\text{B3}) \\ &= \left[ \frac{i\hbar}{2m} \psi_S^e \partial \psi_S^{e*} - v \psi_B^{e*} \psi_A^e \right] - \left[ \frac{i\hbar}{2m} \psi_S^{e*} \partial \psi_S^e + v \psi_A^{e*} \psi_B^e \right]. \end{aligned}$$

Writing  $\psi_S^e = |\psi_S^e| e^{i\theta}$ , we divide by  $|\psi_S^e|$  and use the continuity of the wavefunction at the interface to obtain

$$e^{i\theta} \left[ \frac{i\hbar}{2m} \partial \psi_S^{e*} - v \psi_B^{e*} \right] - e^{-i\theta} \left[ \frac{i\hbar}{2m} \partial \psi_S^e + v \psi_A^e \right] = 0. \quad (\text{B4})$$

Since the overall phase of the wavefunction is arbitrary, this must hold for any  $\theta$ , and thus each term must vanish individually, yielding the boundary condition Eq. (13). For holes in the  $K$  valley, both  $j_{K\text{gr}}^h$  in (B2b) and  $j_S^h$  in (B1b) acquire a minus sign relative to the electron case, and so the result is the same. In the  $K'$  valley, an additional minus sign is present in the expression for the current in graphene, yielding a minus sign in the result. Thus the boundary condition Eq. (13) is established.

### Appendix C: Continuum Calculation of Andreev Reflection at $B = 0$

In this appendix we find a scattering wavefunction for an electron incident from a Dirac material onto a superconductor with parabolic dispersion, following the spirit of the classic BTK analysis [68]. In the superconductor, the wavefunction is given by Eq. (A7), while in the graphene, a solution in the  $K$  valley has the form (A12) where  $\{\phi_i^\beta(y)\}$  are incoming and outgoing plane waves.

At the chemical potential ( $E = 0$ ) the graphene wave-

function is ( $y < 0$ )

$$\begin{aligned} \Psi_{K,k}(y) &= \left[ e^{+ik_y y} \begin{pmatrix} 1 \\ -e^{-i\phi} \end{pmatrix} + r_e e^{-ik_y y} \begin{pmatrix} 1 \\ e^{+i\phi} \end{pmatrix} \right] \otimes \begin{pmatrix} 1 \\ 0 \end{pmatrix} \\ &+ r_h e^{+ik_y y} \begin{pmatrix} 1 \\ -e^{+i\phi} \end{pmatrix} \otimes \begin{pmatrix} 0 \\ 1 \end{pmatrix}, \quad (\text{C1}) \end{aligned}$$

where the wavevector perpendicular to the interface is  $k_y \equiv \sqrt{k_{F\text{gr}}^2 - k^2} > 0$  with  $k_{F\text{gr}} \equiv \mu_{\text{gr}}/\hbar v$ . The phase between the A and B sublattices,  $\phi = \arcsin(k/k_{F\text{gr}}) \in [-\pi/2, +\pi/2]$ , depends on the direction of propagation of the plane wave. From the boundary conditions Eqs. (11)-(13), the four coefficients  $\{r_e, r_h, C_3, C_4\}$  are found. The Andreev reflection probability is then given by  $P_A \equiv |r_h|^2$ . While we focus on the  $E=0$  case here, note that for  $E \neq 0$ , modifications are required:  $k_y$  for the electrons and holes is different, as is the phase  $\phi$  [98]. In the limit  $\Delta \ll \mu_{FS}$  and  $E < \Delta$  these changes typically introduce only a small change in the result.

The matching condition for the wavefunction on the A sublattice yields

$$\begin{pmatrix} 1 + r_e \\ r_h \end{pmatrix} = C_3 \begin{pmatrix} 1 \\ -i \end{pmatrix} + C_4 \begin{pmatrix} 1 \\ +i \end{pmatrix}, \quad (\text{C2})$$

while the current continuity condition results in

$$\begin{pmatrix} e^{-i\phi} - r_e e^{+i\phi} \\ r_h e^{+i\phi} \end{pmatrix} = C_3 \frac{\hbar q}{2mv} \begin{pmatrix} 1 \\ -i \end{pmatrix} - C_4 \frac{\hbar q^*}{2mv} \begin{pmatrix} 1 \\ +i \end{pmatrix}, \quad (\text{C3})$$

in terms of  $q$  defined in Eq. (8). While the imaginary part of  $q$  is crucial for the sense of the problem (it makes the wavefunction in the superconductor evanescent), it is often not very important in determining the relative amplitude of the different contributions because  $\Delta \ll \mu_{FS}$ . So we solve the simplified case  $q = q_y$  first.

*Normal Incidence*,  $q = q_y$ . Initially, we simplify further and consider normal incidence:  $k=0$  and  $\phi=0$ . The solution for the Andreev reflection probability is Eq. (18). In view of (16), the dependence on the graphene Fermi energy is very weak. This is in striking contrast to the case of parabolic dispersion: for normal incidence on an interface between a low-density semiconductor and a superconductor, the result is Eq. (20) [68–71].

*Arbitrary Incidence*,  $q = q_y$ . When not at normal incidence, the solution is

$$P_A = \frac{4\tilde{v}^2 \cos^2 \phi}{1 + \tilde{v}^4 + 2\tilde{v}^2 \cos(2\phi)}. \quad (\text{C4})$$

Note that for all angles of incidence  $\phi$ ,  $P_A = 1$  when  $\tilde{v} = 1$ . The Andreev reflection continues to be smooth, with no strong dependence on either  $q_y$  or  $\phi$ .

*Include imaginary part of  $q$* ,  $q_\Delta^2 \ll q_y^2$ . In most situations,  $k_{FS}$  is not close to  $K$ , and so since  $\Delta \ll \mu_{FS}$ , we have  $q_\Delta^2 \ll q_y^2$ . Then, using the approximation Eq. (9)

for  $q$ , we solve the full  $E = 0$  matching equations and expand to leading order in  $q_\Delta^2/q_y^2$ :

$$P_A = \frac{4\tilde{v}^2 \cos^2 \phi}{1 + \tilde{v}^4 + 2\tilde{v}^2 \cos(2\phi)} \times \left[ 1 - \frac{1}{2} \frac{\tilde{v}^2 (\tilde{v}^2 + \cos(2\phi))}{1 + \tilde{v}^4 + 2\tilde{v}^2 \cos(2\phi)} \left( \frac{q_\Delta^2}{q_y^2} \right)^2 + \dots \right]. \quad (\text{C5})$$

This correction is very small. For instance, for  $\tilde{v} = 1$ ,

$$P_A = \left[ 1 - \frac{1}{4} \left( \frac{q_\Delta^2}{q_y^2} \right)^2 + \dots \right], \quad (\text{C6})$$

independent of the angle of incidence, whereas for normal incidence,

$$P_A = \frac{4\tilde{v}^2}{(1 + \tilde{v}^2)^2} \left[ 1 - \frac{1}{2} \frac{\tilde{v}^2}{1 + \tilde{v}^2} \left( \frac{q_\Delta^2}{q_y^2} \right)^2 + \dots \right]. \quad (\text{C7})$$

These corrections are of order  $(\Delta/\mu_{FS})^2$  and so can be neglected.

*Include imaginary part of  $q$ ,  $q_\Delta^2$  not small.* On the other hand, when the Fermi wavevector in the superconductor is close to matching the valley wavevector in graphene,  $k_{FS} \approx K$ , then the transverse wavevector in the superconductor,  $q_y$ , is small. In that case, the imaginary part of  $q$  is not small, and the approximations in the previous paragraph do not hold.

We start with the case  $q_y = 0$ , implying that  $k_{FS} = p = K + k$ . In this case  $q^2 = i \frac{2m}{\hbar^2} \Delta$  is pure imaginary,

$$q = \frac{\sqrt{2m\Delta}}{\hbar} e^{i\pi/4} \equiv q_\Delta e^{i\pi/4}. \quad (\text{C8})$$

In terms of the scaled  $q_\Delta^2$  defined by

$$\tilde{q}_\Delta^2 = \left( \frac{\hbar q_\Delta}{2mv} \right)^2 = \frac{\Delta}{2mv^2} \ll 1, \quad (\text{C9})$$

the Andreev probability is

$$P_A = \frac{2\tilde{q}_\Delta^2 \cos^2 \phi}{1 + \tilde{q}_\Delta^4 + 2\tilde{q}_\Delta^2 \cos(2\phi)} \approx 2\tilde{q}_\Delta^2 \cos^2 \phi \ll 1. \quad (\text{C10})$$

Thus the Andreev reflection is very small in this limit, of order  $\Delta/\mu_{FS}$ .

Now suppose that  $q_y$  is of order  $q_\Delta$ . Then *both*  $\tilde{v}^2$  and  $\tilde{q}_\Delta^2$  are small. The result will be proportional to either  $\tilde{v}^2$  or  $\tilde{q}_\Delta^2$ , implying that Andreev reflection is weak whenever the imaginary part of  $q$  is significant.

*Summary.* Thus we see that the simple results Eqs. (18) and (C4) provide a good guide to the strength of Andreev reflection, unless  $q_y \lesssim q_\Delta$ . The latter condition in terms of energy is  $\mu_S - \hbar^2(K + k)^2/2m \lesssim \Delta$ : we see that for special fine-tuned values of  $\mu_S$  the Andreev reflection is small. However, in typical situations, we can expect good Andreev reflection at clean graphene-superconductor interfaces.

## Appendix D: Chiral Andreev Edge States in the Continuum Model

In this appendix we show how we obtain the interface modes in the continuum model. First, we fix the form of the transverse wavefunction. It is convenient to introduce the following shifted coordinates and scaled energies:

$$y_\pm \equiv \sqrt{2} (y \pm kl_B^2), \quad \alpha_\pm = \frac{\mu_{gr} \pm E}{E_L}, \quad (\text{D1})$$

where the plus sign pertains to electrons and minus to holes. The functions in Eq. (A12) are [43, 77, 78]

$$\begin{pmatrix} \phi_{1k}^e(y) \\ \phi_{2k}^e(y) \end{pmatrix} = \frac{N_e}{\sqrt{l_B}} \begin{pmatrix} D_{\alpha_+^2}(-y_+/l_B) \\ -i\alpha_+ D_{\alpha_+^2-1}(-y_+/l_B) \end{pmatrix}, \quad (\text{D2})$$

$$\begin{pmatrix} \phi_{1k}^h(y) \\ \phi_{2k}^h(y) \end{pmatrix} = \frac{N_h}{\sqrt{l_B}} \begin{pmatrix} -i\alpha_- D_{\alpha_-^2-1}(-y_-/l_B) \\ D_{\alpha_-^2}(-y_-/l_B) \end{pmatrix}, \quad (\text{D3})$$

where the  $D_n(x)$  are parabolic cylinder functions [99] and  $N_{e,h}$  are normalization coefficients determined by Eq. (A13).

The boundary conditions Eqs. (12)-(13) fix the ratio of the coefficients in the transverse wavefunction. It is convenient to use a scaled wavevector and its real and imaginary parts,

$$\tilde{q} \equiv \frac{\hbar q}{2mv} = \tilde{q}' + i\tilde{q}'', \quad (\text{D4})$$

where  $q$  is defined in Eq. (8). Note that  $\tilde{q}^2 = \tilde{v}^2 + i\Delta/2mv^2$ , but that  $\tilde{q}' \approx \tilde{v}$  only in the approximation  $\Delta \ll \frac{1}{2}mv_y^2$ . The boundary conditions then lead to

$$\frac{C_1}{C_4} = \sqrt{\frac{l_B}{\xi_y}} \frac{2\tilde{q}'}{\tilde{q} \phi_{1k}^e(0) + \phi_{2k}^e(0)}, \quad (\text{D5})$$

$$\frac{C_2}{C_4} = \gamma^* \sqrt{\frac{l_B}{\xi_y}} \frac{2\tilde{q}'}{\phi_{1k}^h(0)\tilde{q} + \phi_{2k}^h(0)}, \quad (\text{D6})$$

$$\frac{C_3}{C_4} = \exp \left[ -2i \arg \left\{ \frac{\tilde{q}}{\phi_{2k}^e(0)} + \frac{1}{\phi_{1k}^e(0)} \right\} \right] \quad (\text{D7})$$

$$= -\exp \left[ -2i \arg \left\{ \frac{\tilde{q}\gamma}{\phi_{2k}^h(0)} + \frac{\gamma}{\phi_{1k}^h(0)} \right\} \right]. \quad (\text{D8})$$

The first two equations imply that the ratio of electron to hole content in graphene is

$$\frac{C_1}{C_2} = \gamma \frac{\tilde{q} \phi_{1k}^h(0) + \phi_{2k}^h(0)}{\tilde{q} \phi_{1k}^e(0) + \phi_{2k}^e(0)} \quad (\text{D9})$$

for the  $K$ -valley mode.

### 1. Secular equation

The secular equation for the spectrum follows from the equality of the electron and hole expressions for  $C_3/C_4$

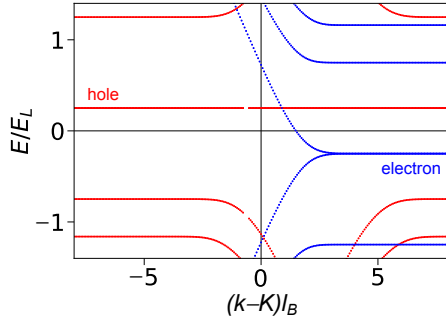


Figure 19. Spectrum of electron (blue) and hole (red) states for a zigzag nanoribbon in the QH regime. Zoom on the  $K$ -valley of the tight-binding results in Fig. 6(c):  $k$  is scaled by  $l_B$  for direct comparison to the continuum results in Fig. 6(a). (Standard parameters, Sec. II D.)

[Eqs. (D7)-(D8)]. It is convenient to define the ratios

$$f_{\pm}(k) \equiv \frac{D_{\alpha_{\pm}^2}(\mp\sqrt{2}kl_B)}{\alpha_{\pm}D_{\alpha_{\pm}^2-1}(\mp\sqrt{2}kl_B)}. \quad (\text{D10})$$

The expressions above for  $C_3/C_4$  in the  $K$  valley lead to

$$|\tilde{q}|^2 f_+ - f_- = \frac{E}{\sqrt{\Delta^2 - E^2}} (f_+ f_- + 1) \tilde{q}' - (f_+ f_- - 1) \tilde{q}''. \quad (\text{D11})$$

By comparing the form of the wavefunction in the  $K$  and  $K'$  valleys, one finds that the corresponding equation for the  $K'$  valley is obtained by the substitution  $f_{\pm} \rightarrow -1/f_{\pm}$ . The same equations are obtained by the substitution  $k \rightarrow -k$  and  $E \rightarrow -E$  in (D11), thus verifying the inherent BdG particle-hole symmetry.

The normal QH edge states (Figs. 3 and 6) can be readily obtained by considering a large barrier at the interface,  $V_0 \rightarrow \infty$  in Eqs. (4) and (14). In that case, (D11) yields  $f_+ = 0$ , which indeed reduces to the usual condition for a QH edge state. As an example of the good quantitative agreement between the continuum and tight-binding models for the QH edge states, in Fig. 19 we show a zoom of the  $K$  valley tight-binding spectrum with  $k$  scaled by  $l_B$  to facilitate comparison with Fig. 6(a).

## 2. Momentum at $E = 0$

Taking  $E = 0$ , we have  $\alpha_+ = \alpha_- \equiv \alpha$  and  $f_+(k_0) = f_-(-k_0)$ . Consider the graphical solution of the secular equation in a very simple limit: ignore the imaginary part of  $\tilde{q}$  completely,  $\tilde{q}'' = 0$ . In this case, the secular equation reduces to

$$f_-(k_0) = \tilde{v}^2 f_+(k_0). \quad (\text{D12})$$

The two sides of this equation (multiplied by the graphene doping) are plotted in Fig. 20 for  $\tilde{v}^2 = 2$  and two values of  $\alpha$ : the right-hand side is simply the mirror image of the left-hand side rescaled by  $\tilde{v}^2$ .

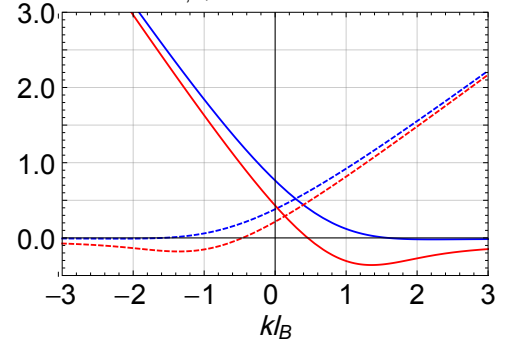


Figure 20. Graphical solution of the transcendental equation  $\alpha f_- = \alpha \tilde{v}^2 f_+$  for the momentum of the  $E = 0$  CAEM: dashed (solid) line for left-hand (right-hand) side. Results for two chemical potentials are shown,  $\alpha = \mu_{\text{gr}}/E_L = 0.25$  (blue) and 0.75 (red). Here,  $\tilde{v}^2 = 2$  and the imaginary part of  $\tilde{q}$  is neglected.

The factor  $\tilde{v}^2$  provides the asymmetry between the electron and hole branches and generally shifts the momentum away from the valley. When  $\tilde{v}^2 = 1$ , the curves are mirror images and so intersect at  $k_0 = 0$  for all  $\alpha$ . This is the valley-degenerate case. On the other hand, when  $\alpha = 1$  (the top of the LLL), the curves go through the origin,  $f_{\pm}(0) = 0$ , and so necessarily intersect there:  $k_0 = 0$  for all  $\tilde{v}^2$  at the top of the LLL. Whether  $\tilde{v}^2 \leq 1$  determines the direction of the momentum shift,  $k_0 \leq 0$ . Finally, the largest possible momentum with  $\alpha$  fixed is given by the uncoupled, terminated-lattice case  $\tilde{v}^2 \rightarrow \infty$ .

## 3. Group velocity

The group velocity of the spectrum at  $E = 0$  has a simple explicit form if one continues to neglect the imaginary part of  $\tilde{q}$ . Implicit differentiation of the secular equation, Eq. (D12), yields

$$\hbar v_g = \frac{\partial E}{\partial k} = \sqrt{2} \mu_{\text{gr}} l_B \frac{\frac{1}{\tilde{v}} + \tilde{v}}{\lambda(\alpha, k_0, \tilde{v}) + E_L/\Delta}, \quad (\text{D13})$$

where the auxiliary function  $\lambda$  is defined by

$$\lambda(\alpha, k_0, \tilde{v}) \equiv - \frac{w(\alpha, z_0)/\tilde{v} + w(\alpha, -z_0)\tilde{v}}{1 + f_+(k_0)f_-(k_0)} \quad (\text{D14})$$

for  $z \equiv \sqrt{2}kl_B$  and

$$w(\alpha, z) \equiv - \frac{f_+}{\alpha} + 2 \frac{1}{D_{\alpha^2-1}(-z)} \partial_{\nu} D_{\nu}(-z)|_{\nu=\alpha^2} - 2 \frac{D_{\alpha^2}(-z)}{D_{\alpha^2-1}^2(-z)} \partial_{\nu} D_{\nu}(-z)|_{\nu=\alpha^2-1}. \quad (\text{D15})$$

We compare these continuum model results to tight-binding calculations for a transparent, well-matched interface in Fig. 21. Despite taking  $\tilde{q}'' = 0$  here, the agreement for dense and sparse stitching is excellent.

We can estimate the change in  $v_g$  between the QH edge states and the fully hybridized CAEM by comparing two

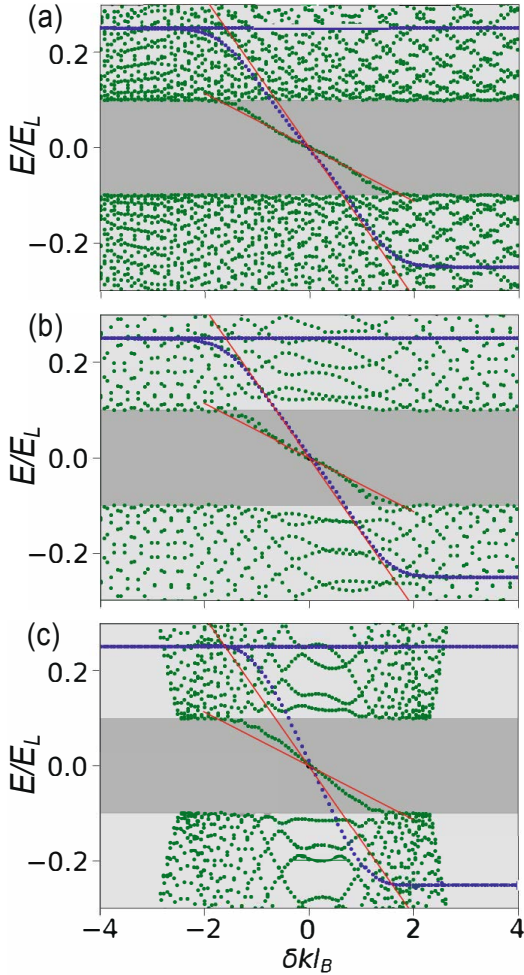


Figure 21. Spectra near the  $K$  point for three transparent tight-binding interfaces—(a) dense, (b) sparse, and (c) honeycomb—compared to the group velocity of the continuum model (red straight lines). Results for two values of the superconducting gap are superposed,  $\Delta/E_L = 0.1$  (green) and  $0.5$  (blue). The continuum model is an excellent description of the tight-binding results. (Standard parameters, Sec. IID.)

limits.  $\lambda(\alpha, k_0, \tilde{v})$  needs to be evaluated at the edge state momentum. However, at good coupling this function is basically flat:  $\lambda(\alpha, 0, 1) \in [2.5, 5]$  from  $\alpha = 0$  to  $1$ . In the disconnected case,  $\tilde{v} \rightarrow \infty$  implies  $\lambda(\alpha, k_0, \tilde{v})/\tilde{v} \rightarrow -w(\alpha, -z_c) \sim 2\alpha + 1/2$ . Taking the ratio yields

$$\frac{v_{g,\text{CAEM}}}{v_{g,\text{QH}}} = \frac{-2w(\alpha, -z_0)}{\lambda(\alpha, 0, 1) + E_L/\Delta} \sim \frac{1 + 4\mu_{\text{gr}}/E_L}{\lambda(\alpha, 0, 1) + E_L/\Delta}. \quad (\text{D16})$$

Thus we see that the Andreev edge modes in the typical case  $E_L \gg \Delta$  are substantially slower. For strong magnetic quantization ( $E_L/\Delta \gg \lambda$ ), a good estimate of the CAEM group velocity is

$$\frac{\hbar v_{g,\text{CAEM}}}{l_B} \sim \sqrt{2}\Delta \left( \frac{1}{|\tilde{q}|} + |\tilde{q}| \right) \frac{\mu_{\text{gr}}}{E_L}, \quad (\text{D17})$$

proportional to the pairing gap and a factor characterizing interface quality.

- 
- [1] C. W. J. Beenakker, Colloquium: Andreev reflection and Klein tunneling in graphene, *Rev. Mod. Phys.* **80**, 1337 (2008).
  - [2] G.-H. Lee and H.-J. Lee, Proximity coupling in superconductor-graphene heterostructures, *Rep. Prog. Phys.* **81**, 056502 (2018).
  - [3] B. J. van Wees and H. Takayanagi, The superconducting proximity effect in semiconductor-superconductor systems: Ballistic transport, low dimensionality, and sample specific properties, in *Mesoscopic Electron Transport*, edited by L. L. Sohn, L. P. Kouwenhoven, and G. Schön (Kluwer, Dordrecht, Netherlands, 1997) pp. 469–501.
  - [4] Y.-J. Doh, J. A. van Dam, A. L. Roest, E. P. A. M. Bakkers, L. P. Kouwenhoven, and S. De Franceschi, Tunable supercurrent through semiconductor nanowires, *Science* **309**, 272 (2005).
  - [5] T. Akazaki, H. Takayanagi, J. Nitta, and T. Enoki, A Josephson field effect transistor using an InAs-inserted-channel  $\text{In}_{0.52}\text{Al}_{0.48}\text{As}/\text{In}_{0.53}\text{Ga}_{0.47}\text{As}$  inverted modulation-doped structure, *Appl. Phys. Lett.* **68**, 418 (1996).
  - [6] F. Wen, J. Shabani, and E. Tutuc, Josephson junction field-effect transistors for Boolean logic cryogenic applications, *IEEE Trans. Elec. Dev.* **66**, 5367 (2019).
  - [7] D. Phan, P. Falthansl-Scheinecker, U. Mishra, W. M. Strickland, D. Langone, J. Shabani, and A. P. Higginbotham, Gate-tunable superconductor-semiconductor parametric amplifier, *Phys. Rev. Appl.* **19**, 064032 (2023).
  - [8] B. Huang, E. G. Arnault, W. Jung, C. Fried, B. J. Russell, K. Watanabe, T. Taniguchi, E. A. Henriksen, D. Englund, G.-H. Lee, and K. C. Fong, *Graphene calorimetric single-photon detector* (2024), arXiv:2410.22433.
  - [9] C. R. Dean, A. F. Young, I. Meric, C. Lee, L. Wang,

- S. Sorgenfrei, K. Watanabe, T. Taniguchi, P. Kim, K. L. Shepard, and J. Hone, Boron nitride substrates for high-quality graphene electronics, *Nat. Nano.* **5**, 722 (2010).
- [10] A. S. Mayorov, R. V. Gorbachev, S. V. Morozov, L. Britnell, R. Jalil, L. A. Ponomarenko, P. Blake, K. S. Novoselov, K. Watanabe, T. Taniguchi, and A. K. Geim, Micrometer-scale ballistic transport in encapsulated graphene at room temperature, *Nano Lett.* **11**, 2396 (2011).
- [11] L. Wang, I. Meric, P. Y. Huang, Q. Gao, Y. Gao, H. Tran, T. Taniguchi, K. Watanabe, L. M. Campos, D. A. Muller, J. Guo, P. Kim, J. Hone, K. L. Shepard, and C. R. Dean, One-dimensional electrical contact to a two-dimensional material, *Science* **342**, 614 (2013).
- [12] A. F. Young, C. R. Dean, L. Wang, H. Ren, P. Cadden-Zimansky, K. Watanabe, T. Taniguchi, J. Hone, K. L. Shepard, and P. Kim, Spin and valley quantum Hall ferromagnetism in graphene, *Nat. Phys.* **8**, 550 (2012).
- [13] V. E. Calado, S. Goswami, G. Nanda, M. Diez, A. R. Akhmerov, K. Watanabe, T. Taniguchi, T. M. Klapwijk, and L. M. K. Vandersypen, Ballistic Josephson junctions in edge-contacted graphene, *Nat. Nano.* **10**, 761 (2015).
- [14] M. Ben Shalom, M. J. Zhu, V. I. Fal'ko, A. Mishchenko, A. V. Kretinin, K. S. Novoselov, C. R. Woods, K. Watanabe, T. Taniguchi, A. K. Geim, and J. R. Prance, Quantum oscillations of the critical current and high-field superconducting proximity in ballistic graphene, *Nat. Phys.* **12**, 318 (2016).
- [15] F. Amet, C. T. Ke, I. V. Borzenets, J. Wang, K. Watanabe, T. Taniguchi, R. S. Deacon, M. Yamamoto, Y. Bomze, S. Tarucha, and G. Finkelstein, Supercurrent in the quantum Hall regime, *Science* **352**, 966 (2016).
- [16] G.-H. Park, M. Kim, K. Watanabe, T. Taniguchi, and H.-J. Lee, Propagation of superconducting coherence via chiral quantum-Hall edge channels, *Sci. Rep.* **7**, 10953 (2017).
- [17] G.-H. Lee, K.-F. Huang, D. K. Efetov, D. S. Wei, S. Hart, T. Taniguchi, K. Watanabe, A. Yacoby, and P. Kim, Inducing superconducting correlation in quantum Hall edge states, *Nat. Phys.* **13**, 693 (2017).
- [18] M. R. Sahu, X. Liu, A. K. Paul, S. Das, P. Raychaudhuri, J. K. Jain, and A. Das, Inter-Landau-level Andreev reflection at the Dirac point in a graphene quantum Hall state coupled to a NbSe<sub>2</sub> superconductor, *Phys. Rev. Lett.* **121**, 086809 (2018).
- [19] H. Vignaud, D. Perconte, W. Yang, B. Kousar, E. Wagner, F. Gay, K. Watanabe, T. Taniguchi, H. Courtois, Z. Han, H. Sellier, and B. Sacépé, Evidence for chiral supercurrent in quantum Hall Josephson junctions, *Nature* **624**, 545 (2023), arXiv:2305.01766.
- [20] J. Alicea, New directions in the pursuit of Majorana fermions in solid state systems, *Rep. Prog. Phys.* **75**, 076501 (2012).
- [21] C. W. J. Beenakker, Search for Majorana fermions in superconductors, *Ann. Rev. Cond. Matt. Phys.* **4**, 113 (2013).
- [22] X.-L. Qi, T. L. Hughes, and S.-C. Zhang, Chiral topological superconductor from the quantum Hall state, *Phys. Rev. B* **82**, 184516 (2010).
- [23] R. S. K. Mong, D. J. Clarke, J. Alicea, N. H. Lindner, P. Fendley, C. Nayak, Y. Oreg, A. Stern, E. Berg, K. Shtengel, and M. P. A. Fisher, Universal topological quantum computation from a superconductor-Abelian quantum Hall heterostructure, *Phys. Rev. X* **4**, 011036 (2014).
- [24] B. Lian, X.-Q. Sun, A. Vaezi, X.-L. Qi, and S.-C. Zhang, Topological quantum computation based on chiral Majorana fermions, *PNAS* **115**, 10938 (2018).
- [25] I. V. Borzenets, F. Amet, C. T. Ke, A. W. Draelos, M. T. Wei, A. Seredinski, K. Watanabe, T. Taniguchi, Y. Bomze, M. Yamamoto, S. Tarucha, and G. Finkelstein, Ballistic graphene Josephson junctions from the short to the long junction regimes, *Phys. Rev. Lett.* **117**, 237002 (2016).
- [26] J. Park, J. H. Lee, G.-H. Lee, Y. Takane, K.-I. Imura, T. Taniguchi, K. Watanabe, and H.-J. Lee, Short ballistic Josephson coupling in planar graphene junctions with inhomogeneous carrier doping, *Phys. Rev. Lett.* **120**, 077701 (2018).
- [27] A. Seredinski, A. W. Draelos, E. G. Arnault, M.-T. Wei, H. Li, T. Fleming, K. Watanabe, T. Taniguchi, F. Amet, and G. Finkelstein, Quantum Hall-based superconducting interference device, *Sci. Adv.* **5**, eaaw8693 (2019), arXiv:1901.05928.
- [28] L. Zhao, E. G. Arnault, T. F. Q. Larson, K. Watanabe, T. Taniguchi, F. Amet, and G. Finkelstein, Non-local transport measurements in hybrid quantum Hall-superconducting devices, *Phys. Rev. B* **109**, 115416 (2024), arXiv:2310.02910.
- [29] L. Zhao, E. G. Arnault, A. Bondarev, A. Seredinski, T. F. Q. Larson, A. W. Draelos, H. Li, K. Watanabe, T. Taniguchi, F. Amet, H. U. Baranger, and G. Finkelstein, Interference of chiral Andreev edge states, *Nat. Phys.* **16**, 862 (2020), arXiv:1907.01722.
- [30] L. Zhao, Z. Iftikhar, T. F. Larson, E. G. Arnault, K. Watanabe, T. Taniguchi, F. Amet, and G. Finkelstein, Loss and decoherence at the quantum Hall-superconductor interface, *Phys. Rev. Lett.* **131**, 176604 (2023), arXiv:2210.04842.
- [31] M. R. Sahu, A. K. Paul, J. Sutradhar, K. Watanabe, T. Taniguchi, V. Singh, S. Mukerjee, S. Banerjee, and A. Das, Quantized conductance with nonzero shot noise as a signature of Andreev edge state, *Phys. Rev. B* **104**, L081404 (2021), arXiv:2105.13070.
- [32] L. Zhao, T. F. Q. Larson, Z. Iftikhar, J. Chiles, K. Watanabe, T. Taniguchi, F. Amet, and G. Finkelstein, *Thermal properties of the superconductor-quantum Hall interfaces* (2024), arXiv:2406.00850.
- [33] M. J. Zhu, A. V. Kretinin, M. D. Thompson, D. A. Bandurin, S. Hu, G. L. Yu, J. Birkbeck, A. Mishchenko, I. J. Vera-Marun, K. Watanabe, T. Taniguchi, M. Polini, J. R. Prance, K. S. Novoselov, A. K. Geim, and M. Ben Shalom, Edge currents shunt the insulating bulk in gapped graphene, *Nat. Comm.* **8**, 14552 (2017).
- [34] C. T. Ke, A. W. Draelos, A. Seredinski, M. T. Wei, H. Li, M. Hernandez-Rivera, K. Watanabe, T. Taniguchi, M. Yamamoto, S. Tarucha, Y. Bomze, I. V. Borzenets, F. Amet, and G. Finkelstein, Anomalous periodicity of magnetic interference patterns in encapsulated graphene Josephson junctions, *Phys. Rev. Res.* **1**, 033084 (2019).
- [35] J. Eroms, D. Weiss, J. D. Boeck, G. Borghs, and U. Zülicke, Andreev reflection at high magnetic fields: Evidence for electron and hole transport in edge states, *Phys. Rev. Lett.* **95**, 107001 (2005).
- [36] Y. Kozuka, A. Sakaguchi, J. Falson, A. Tsukazaki, and M. Kawasaki, Andreev reflection at the interface with an oxide in the quantum Hall regime, *J. Phys. Soc. Jpn.* **87**, 124712 (2018), arXiv:1810.08198.
- [37] S. Matsuo, K. Ueda, S. Baba, H. Kamata, M. Tateno, J. Shabani, C. J. Palmstrøm, and S. Tarucha, Equal-spin

- Andreev reflection on junctions of spin-resolved quantum Hall bulk state and spin-singlet superconductor, *Sci. Rep.* **8**, 3454 (2018).
- [38] M. Hatefipour, J. J. Cuzzo, J. Kanter, W. M. Strickland, C. R. Allemang, T.-M. Lu, E. Rossi, and J. Shabani, Induced superconducting pairing in integer quantum Hall edge states, *Nano Lett.* **22**, 6173 (2022), arXiv:2108.08899.
- [39] M. Hatefipour, J. J. Cuzzo, I. Levy, W. M. Strickland, D. Langone, E. Rossi, and J. Shabani, Andreev reflection of quantum Hall states through a quantum point contact, *Phys. Rev. B* **109**, 035430 (2024), arXiv:arXiv:2309.01856.
- [40] M. Ma and A. Y. Zyuzin, Josephson effect in the quantum Hall regime, *Europhys. Lett.* **21**, 941 (1993).
- [41] A. Y. Zyuzin, Superconductor–normal-metal–superconductor junction in a strong magnetic field, *Phys. Rev. B* **50**, 323 (1994).
- [42] Y. Takagaki, Transport properties of semiconductor–superconductor junctions in quantizing magnetic fields, *Phys. Rev. B* **57**, 4009 (1998).
- [43] H. Hoppe, U. Zülicke, and G. Schön, Andreev reflection in strong magnetic fields, *Phys. Rev. Lett.* **84**, 1804 (2000).
- [44] U. Zülicke, H. Hoppe, and G. Schön, Andreev reflection at superconductor–semiconductor interfaces in high magnetic fields, *Physica B* **298**, 453 (2001).
- [45] F. Giazotto, M. Governale, U. Zülicke, and F. Beltram, Andreev reflection and cyclotron motion at superconductor–normal-metal interfaces, *Phys. Rev. B* **72**, 054518 (2005).
- [46] I. M. Khaymovich, N. M. Chitchev, I. A. Shereshevskii, and A. S. Mel'nikov, Andreev transport in two-dimensional normal–superconducting systems in strong magnetic fields, *Europhys. Lett.* **91**, 17005 (2010).
- [47] M. Stone and Y. Lin, Josephson currents in quantum Hall devices, *Phys. Rev. B* **83**, 224501 (2011).
- [48] J. A. M. van Ostaay, A. R. Akhmerov, and C. W. J. Beenakker, Spin-triplet supercurrent carried by quantum Hall edge states through a Josephson junction, *Phys. Rev. B* **83**, 195441 (2011).
- [49] B. Lian, J. Wang, and S.-C. Zhang, Edge-state-induced Andreev oscillation in quantum anomalous Hall insulator–superconductor junctions, *Phys. Rev. B* **93**, 161401 (2016).
- [50] O. Gamayun, J. A. Hutasoit, and V. V. Cheianov, Two-terminal transport along a proximity-induced superconducting quantum Hall edge, *Phys. Rev. B* **96**, 241104 (2017).
- [51] Y. Alavirad, J. Lee, Z.-X. Lin, and J. D. Sau, Chiral supercurrent through a quantum Hall weak link, *Phys. Rev. B* **98**, 214504 (2018).
- [52] M. Beconcini, M. Polini, and F. Taddei, Nonlocal superconducting correlations in graphene in the quantum Hall regime, *Phys. Rev. B* **97**, 201403 (2018).
- [53] A. Manesco, I. M. Flór, C.-X. Liu, and A. Akhmerov, Mechanisms of Andreev reflection in quantum Hall graphene, *SciPost Phys. Core* **5**, 045 (2022), arXiv:2103.06722.
- [54] L. Peralta Gavensky, G. Usaj, and C. A. Balseiro, Nonequilibrium edge transport in quantum Hall based Josephson junctions, *Phys. Rev. B* **103**, 024527 (2021), arXiv: 2010.13805.
- [55] Y. Tang, C. Knapp, and J. Alicea, Vortex-enabled Andreev processes in quantum Hall–superconductor hybrids, *Phys. Rev. B* **106**, 245411 (2022).
- [56] T. H. Galambos, F. Ronetti, B. Hetényi, D. Loss, and J. Klinovaja, Crossed Andreev reflection in spin-polarized chiral edge states due to the Meissner effect, *Phys. Rev. B* **106**, 075410 (2022), arXiv:2203.05894.
- [57] V. D. Kurilovich, Z. M. Raines, and L. I. Glazman, Disorder in Andreev reflection of a quantum Hall edge, *Nat. Comm.* **14**, 2237 (2023), arXiv:2201.00273.
- [58] A. B. Michelsen, P. Recher, B. Braunecker, and T. L. Schmidt, Supercurrent-enabled Andreev reflection in a chiral quantum Hall edge state, *Phys. Rev. Res.* **5**, 013066 (2023), arXiv:2203.13384.
- [59] A. David, J. S. Meyer, and M. Houzet, Geometrical effects on the downstream conductance in quantum-Hall–superconductor hybrid systems, *Phys. Rev. B* **107**, 125416 (2023), arXiv:2210.16867.
- [60] N. Schiller, B. A. Katzir, A. Stern, E. Berg, N. H. Lindner, and Y. Oreg, Superconductivity and fermionic dissipation in quantum Hall edges, *Phys. Rev. B* **107**, L161105 (2023), arXiv:2202.10475.
- [61] V. Khrapai, Quantum Hall Bogoliubov interferometer, *Phys. Rev. B* **107**, L241401 (2023), arXiv:2210.05525.
- [62] J. J. Cuzzo and E. Rossi, SU(4) symmetry breaking and induced superconductivity in graphene quantum Hall edges, *Phys. Rev. B* **110**, 024518 (2024), arXiv:2306.12483.
- [63] Y. Hu, J. Wang, and B. Lian, *Resistance distribution of decoherent quantum Hall–superconductor edges* (2024), arXiv:2405.17550 [cond-mat].
- [64] P. G. de Gennes, *Superconductivity of Metals and Alloys* (Perseus Books Publishing, Reading, Massachusetts, 1966).
- [65] T. M. Klapwijk, Proximity effect from an Andreev perspective, *J. Supercond.* **17**, 593 (2004).
- [66] Y. Asano, *Andreev Reflection in Superconducting Junctions*, Springer Briefs in Physics (Springer, Singapore, 2021).
- [67] P. Coleman, *Introduction to Many-Body Physics* (Cambridge Univ. Press, Cambridge UK, 2015) p.500.
- [68] G. E. Blonder, M. Tinkham, and T. M. Klapwijk, Transition from metallic to tunneling regimes in superconducting microconstrictions: Excess current, charge imbalance, and supercurrent conversion, *Phys. Rev. B* **25**, 4515 (1982).
- [69] G. E. Blonder and M. Tinkham, Metallic to tunneling transition in Cu-Nb point contacts, *Phys. Rev. B* **27**, 112 (1983).
- [70] H. Nakano and H. Takayanagi, Quasiparticle interferometer controlled by quantum-correlated Andreev reflection, *Phys. Rev. B* **47**, 7986 (1993).
- [71] N. A. Mortensen, K. Flensberg, and A.-P. Jauho, Angle dependence of Andreev scattering at semiconductor–superconductor interfaces, *Phys. Rev. B* **59**, 10176 (1999).
- [72] The solutions in the lower left and upper right of Fig. 1(c) are at the energy of the superconducting gap and so not relevant for our discussion of the CAEM.
- [73] A. R. Akhmerov and C. W. J. Beenakker, Boundary conditions for Dirac fermions on a terminated honeycomb lattice, *Phys. Rev. B* **77**, 085423 (2008).
- [74] J. A. M. van Ostaay, A. R. Akhmerov, C. W. J. Beenakker, and M. Wimmer, Dirac boundary condition at the reconstructed zigzag edge of graphene, *Phys. Rev. B* **84**, 195434 (2011).

- [75] Y. M. Blanter and I. Martin, Transport through normal-metal-graphene contacts, *Phys. Rev. B* **76**, 155433 (2007).
- [76] Y. Takagaki, Quantum magnetotransport oscillations in graphene nanoribbons coupled to superconductors, *J. Phys. Cond. Matt.* **33**, 255301 (2021).
- [77] A. R. Akhmerov and C. W. J. Beenakker, Detection of valley polarization in graphene by a superconducting contact, *Phys. Rev. Lett.* **98**, 157003 (2007).
- [78] I. Romanovsky, C. Yannouleas, and U. Landman, Unique nature of the lowest Landau level in finite graphene samples with zigzag edges: Dirac electrons with mixed bulk-edge character, *Phys. Rev. B* **83**, 045421 (2011).
- [79] This can be shown by placing the barrier inside the superconductor at an arbitrary position  $y_0$ , integrating across the  $\delta$ -function as usual for parabolic dispersion, and then taking the limit  $y_0 \rightarrow 0$  [68, 69].
- [80] The width of the zigzag graphene nanoribbon is  $y_{QH} = \frac{300}{\sqrt{3}}a$ . The width of the superconductor is, respectively,  $y_S = 150a$ ,  $400a$ , and  $\frac{300}{\sqrt{3}}a$  for our dense, sparse, and honeycomb results.
- [81] A. David, *Chiral and Helical Boundary Modes Coupled to a Superconductor*, Ph.D. thesis, Université Grenoble Alpes (2023), p. 164.
- [82] L. Brey and H. A. Fertig, Edge states and the quantized Hall effect in graphene, *Phys. Rev. B* **73**, 195408 (2006).
- [83] A. H. Castro Neto, F. Guinea, and N. M. R. Peres, Edge and surface states in the quantum Hall effect in graphene, *Phys. Rev. B* **73**, 205408 (2006).
- [84] P. Delplace and G. Montambaux, WKB analysis of edge states in graphene in a strong magnetic field, *Phys. Rev. B* **82**, 205412 (2010).
- [85] A. H. Castro Neto, F. Guinea, N. M. R. Peres, K. S. Novoselov, and A. K. Geim, The electronic properties of graphene, *Rev. Mod. Phys.* **81**, 109 (2009).
- [86] More precisely, for quantities (ii) and (iii) one must take the projection perpendicular to the interface [see Eq. (8)]: for (ii), the period of the oscillations is  $2\pi/q' \approx 2\pi/q_y$ , and for (iii), the coherence length perpendicular to the interface is  $\xi_y \equiv 1/q'' \approx \hbar v_y/\Delta$  which, for small  $\Delta$ , is much larger than the period. The rapid oscillations of the electron and hole wavefunctions in the superconductor are exactly out of phase, as expected for a mid-gap state ( $E = 0$  implies  $\gamma = -i$ ).
- [87] For a precise evaluation of the *transparency* here (in contrast to our loose use of the term “transparent”), consider the honeycomb-to-square-lattice interface in the absence of both superconductivity and a magnetic field. We find the transmission per mode from the graphene to the superconductor using a simple two-terminal nanoribbon geometry. For fixed interface parameters, the transparency is this transmission probability averaged over a few nanoribbon widths.
- [88] The decay of  $\psi_S$  is slower in Fig. 5(b) than in (a) because the lattice constant is double that in the dense case.
- [89] In looking at such BdG spectra one must keep in mind the inherent redundancy due to the doubling of the degrees of freedom.
- [90] The choice  $W \lesssim l_B^2(4\pi/3a)$  avoids having the spectrum of the bulk states wrap around the Brillouin zone, which would then overlap the spectrum of the edge states near  $y=0$ .
- [91] T. Ihn, *Semiconductor Nanostructures* (Oxford Univ. Press, Oxford UK, 2010) p. 311.
- [92] In the continuum model, such a deviation of the propagating mode at the chemical potential,  $\delta k_0$  is obtained for  $\tilde{v}^2 = 0.38$  and  $0.41$ , respectively.
- [93] Our convention for labeling the spin of the Andreev reflected hole follows that for the linear momentum: an incoming spin up particle forms a Cooper pair with a spin down particle. The missing spin down angular momentum implies that the Andreev reflected hole is spin up. Thus an incoming electron Andreev reflects into a hole in the same valley with the same spin [67].
- [94] K. Nomura and A. H. MacDonald, Quantum Hall ferromagnetism in graphene, *Phys. Rev. Lett.* **96**, 256602 (2006).
- [95] M. O. Goerbig, Electronic properties of graphene in a strong magnetic field, *Rev. Mod. Phys.* **83**, 1193 (2011).
- [96] A. Bondarev, G. Zhang, and H. U. Baranger, *Data for “Transparent Graphene-Superconductor Interfaces: Quantum Hall and Zero Field Regimes”* (2025).
- [97] C. W. Groth, M. Wimmer, A. R. Akhmerov, and X. Waintal, Kwant: A software package for quantum transport, *New J. Phys.* **16**, 063065 (2014).
- [98] In addition, we have suppressed a factor that may be important in other situations. Strictly speaking, one should consider input and output beams that all have the same current; thus, the plane waves in Eq. (C1) should be divided by  $\sqrt{\cos\phi}$ . In our situation, different wavevectors are not mixed, so this is the same for all components (at  $E = 0$ ). If the interface were to cause momentum mixing, then this effect must be included.
- [99] N. M. Temme, Parabolic cylinder functions, in *NIST Handbook of Mathematical Functions*, edited by F. W. J. Oliver, D. W. Lozier, R. F. Boisvert, and C. W. Clark (Cambridge Univ. Press, Cambridge UK, 2010) pp. 303–319.